Electron Transport in Single-Walled Carbon Nanotubes

Meninder S. Purewal

Submitted in partial fulfillment of the
Requirements for the degree
of Doctor of Philosophy
in the Fu Foundation of
Engineering and Applied Science

COLUMBIA UNIVERSITY

2008

Abstract

Electron Transport in Single-Walled Carbon Nanotubes

Meninder S. Purewal

We present electron transport experiments on single walled carbon nanotubes (SWNTs). By measuring the linear scaling of resistance with length, we determine an unusually long mean free path of $L_m \sim 1$ μm at room temperature. From the temperature dependence of the mean free path for over 10 samples we show that inelastic scattering with acoustic phonons are the main source of scattering at room temperature and experimentally determine the electron-acoustic phonon strength. Disorder ultimately limits the low temperature mean free path ($L_m \sim 10$ μm), which we show by employing scanning gate microscopy. We analyze the non-linear scaling of resistance with length and temperature to further elucidate the nature of this disorder. In general, we find that transport in 1-dimension is dominated by the strongest defect along the channel. For larger source-drain voltage ($V_{SD} > 0.2$ V), we show that L_m is significantly reduced in both metallic and semiconducting SWNTs, due to electrons scattering with the higher energy phonons. In semiconducting samples, when the Fermi energy is close to the energy band gap, we observe an anomalous conductance dip. Finally, we utilize locally controlled gate structures to fabricate a series of tunable barriers to form a superlattice and observe its mini-band structure superimposed on that of the nanotubes.

Contents

List of Figures

List of Tables

Acknowledgements

This thesis describes experiments that took place during my 5 years of research at Columbia University. There are so many people that have contributed both directly and indirectly to this body of work. First of all, I would like to thank my advisor Philip Kim, who I met before I enrolled in Columbia. Despite the busy schedule of a professor, Philip was kind enough to take time out and help me think through critical decisions on which schools to apply to and later, which to accept. As a thesis advisor he was no different - from taking time to explain voltage dividers to the most complex physics, Philip always seemed to know how to break down concepts so that I could understand. Looking back to my first year of research, I see how much Philip has taught me directly and influenced my critical thinking skills. I feel extremely fortunate to have worked in his lab. He is easy to talk and it is to his credit that he creates such a dynamic lab environment. Members have the flexibility to pursue their own ideas and this contributes to the exciting (and fun) work environment.

Which leads to my lab colleagues, who made my time at Columbia memorable. Thanks to the former lab members Josh Small, Yuanbo Zhang, Alex Henderson who introduced me to fabrication and low dimensional physics. To post-doc Byung-Hee Hong- thanks for the amazing ultra-long nanotubes that made my experiments possible. To post-doc Barbaros Oezyilmaz, who was the funniest person I met at Columbia. He was always around for some brotherly advice about both life and science (and places to eat and gifts ideas). To post-doc Pablo Jarillo-Herrero, who I learned a lot from when fabricating the superlattice. To post-doc Kirill Bolotin (second funniest?) and Erik Henriksen, who each had magic fabrication fingers and

were always willing to listen to my fabrication/measurement problems and make suggestions. Finally, all the graduate students in the Kim group. The favors we do each other on a daily basis is easy to overlook, but is a great aspect of our lab. I have gotten to know Melinda Han and Yuri Zuev very well and will miss our lunches and coffee/cookie breaks. Also thanks for the exciting experience of working with my talented fellow lab members Andrea Young, Dmitri Efetov, Mitsu Takekoshi, Yue Zhao, and Nan Lin. I look forward to reading about your future research accomplishments. I have also been fortunate enough to work with very talented undergraduates- Asher Mullokandov, Ani Ravi, Joel Chudow, and Xi Guo.

Thanks to Professor Irving Herman for his active interest in my research and overall standing through my years at Columbia. To Professor Aron Pinczuk, who was the instructor for my first Solid State Physics course and allowed me to TA it thereafter. To Professor Jim Hone for being available to talk nanotubes, and his lab members Bhupesh Chandra and Robert Caldwell. And to Professor Jim Yardley for his "big picture" discussions. I probably would not have even pursued a Ph.D if it were not for my undergraduate advisor at Lehigh, Professor Yong Kim, who encouraged me by believing in my ability to do physics.

My years at Columbia would not have been the same without two friends I made my first year: Thomas Kirschenmann and Eric Raleigh. Thomas, I will always remember the walks from 120th Street to Times Square looking for a place to eat. (We would never find a suitable cuisine so we would take the train back to CU and eat at Tom's Restaurant.) Eric was my roommate for two, completely unforgettable years (well, maybe some parts I can't remember). Both are my great lifelong friends that I have to thank for being around for some of the more difficult parts of my research years.

Blake Feldman was always interested in my research and I would look forward to the physics (and non-physics) discussions we had that reminded me of why I found physics exciting in the first place. My "Staten Island" friends Sean Markowitz, Brandon Ginsburg, and Neal Ziskind were always around when I needed to blow off some steam and were understanding when they wouldn't see me for months at

a time. Thanks also to Craig Sabbatino for those occasional, yet certain pow-wow meals where would catch up on each other's life. And to K.C. Wennogle, who let me stay at his place in Denver during March Meeting 2007 and taught me the plural of Guinness (Guinnei).

To my brother and sister, who made it abundantly clear they were available for anything big or small. Even when this safety net went unused, it allowed me to accomplish more than I would have normally been capable of doing. Thanks for always "being there". Thanks to their spouses, Rakhi and Joe, who have expanded this network of support and have made our family larger and even more joyous. I am looking forward to the days when, the newest additions to our family, my nieces Sanya and Tanseem and nephew Harnek grow up and I can teach them physics.

To my father, whose curiosity and desire for fundamental understanding of the world I inherited. Thank you for the "blank check" and unlimited support you gave me in life that allowed me choose whatever path I wanted. Your support for my actions are instrumental to me completing my PhD. To my mother, who I owe a lot of tupperware to. She would always make sure I had enough to eat by packing a week of meals for me. It was one of the many ways she showed she cared and supported me while I worked on my PhD. She also made sure I remained grounded and never failed to stress the importance of family to me. I dedicate my PhD to my mother and father in return for the infinite love and support they provided.

Finally, to Pooja, who has been my best friend and steadfast supporter for the last seven years. Her unwavering belief in my ability encouraged me during the tougher times. Thank you for all the times when you told me: "You can do it". I did it! I will always be fond of my memories and the people I met at Columbia. As this chapter closes, I am excited about the new chapter that begins when Pooja and I get married in a few weeks.

Meninder Purewal May 2008

To my Father and my Mother

Chapter 1

Introduction to Electron Transport in Single-Walled Carbon Nanotubes

1.1 Wide World of Carbon Nanotubes

Carbon nanotubes are the one dimensional (1D) member of carbon's sp^2 bonding family. The three dimensional counterpart of nanotubes is the material graphite (Figure 1.1), which has been known to exist prior to 1600 [1]. In 1985, the zero-dimensional structure known as the fullerene molecule was discovered [2]. Shortly after in 1991, Sumio Iijima discovered that by exposing carbon material to a high

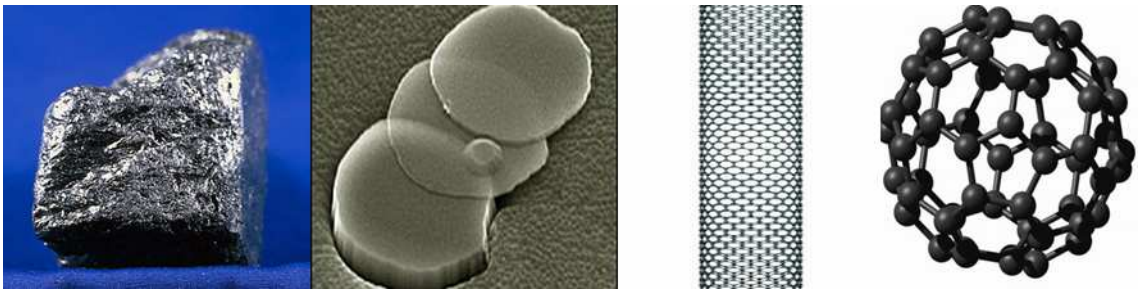

Figure 1.1: From left to right: Graphite, Graphene, Carbon Nanotubes, and the Fullerene. These are the 3, 2, 1, and 0 dimensional structures of the carbon sp^2 family.

temperature environment, one-dimensional carbon nanotubes are synthesized [3]. Recently in 2004, it was discovered that by micro-mechanically cleaving graphite, a single layer of graphite, or two-dimensional graphene can be obtained [4]. With the exception of bulk graphite, it is amusing to think that carbon materials were discovered from the lowest dimensional structures (fullerenes) to successively higher dimensional forms (nanotubes and then graphene).

This thesis will cover electron transport in 1D carbon nanotubes (CNTs). CNTs have the shape of a cylinder with a diameter of about 1 nm and length that can exceed 10 cm [5] - an aspect ratio of 10^8! (see Figure 1.7(c)). They are known to be remarkably strong and lightweight; they are the stiffest materials in nature with a tensile strength in the 10's of gigapascals [6]. This feature has contributed to the use of carbon nanotubes in commercial products such as baseball bats, tennis rackets, and even paint, where it is boasted that the CNT's make its host stronger and more stable, while not contributing significantly to the weight. The strength is derived in part from the strong covalent bonding between carbon atoms.

Besides outstanding mechanical characteristics, another motivation for the study of CNTs has been their electrical properties. For multiple reasons they show promise as the replacement to the solid state transistor pervasively used in modern electronics. This includes : (i) Current densities can exceed 10^9 Amps/cm^2 without breakdown due to electromigration [7]. This is an order of magnitude greater than the current density tolerance of copper. (ii) CNTs have an unusually long mean free path at room temperature (1 μm) [8]. This allows for the possibility of ballistic conduction at RT, and thus lower power dissipation. It also allows for the exploitation of quantum mechanical phenomena at room temperature. (iii) CNTs can either be metallic or semiconducting, with an energy band gap inversely proportional to its diameter, a property that is a direct result of the electrical properties of the parent structure graphene. Semiconducting CNTs have been shown to exhibit transistor-like behavior with on/off ratios of 10^5 [9]. This allows for the possibility of an entire circuit to be built from CNTs, where metallic CNTs serve as interconnects to the semiconducting CNTs, which serve as transistors.

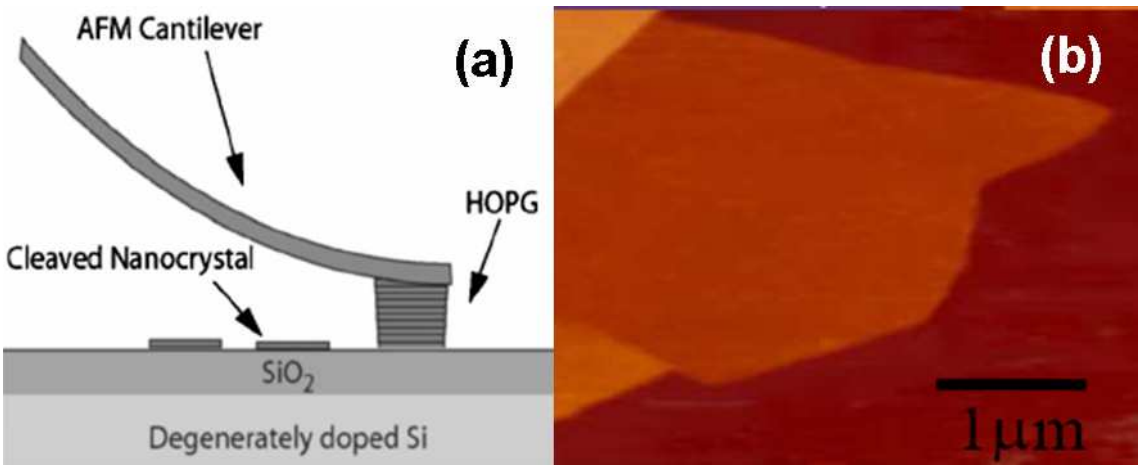

Figure 1.2: (a) Zhang et al. used a sophisticated micro-mechanical cleaving technique (nano-pencil) to extract few layer graphite (from Ref. [10]). (b) Atomically thin graphene was obtained around the same time using a relatively low-tech manner - with ordinary Scotch tape [4].

Combining all these features, CNTs show significant promise for future use in nanoelectronics. Besides practical uses, they offer an intriguing and exciting window into 1D physics and quantum mechanics. The relatively recent innovations of microscopy tools like scanning probe and scanning electron allows us to probe this world as was never possible before.

1.2 A Word on Graphene

It is impossible to discuss CNTs faithfully without first addressing the recent breakthrough with graphene. When I began my research in 2004, CNTs were the material of choice for many scientists in the experimental condensed matter community. It provided an obvious choice to study myriad fundamental 1D and quantum mechanical physics, with the upside of potential nanotechnology applications. In Professor Kim's lab, where I was a member, my colleague Yuanbo Zhang was not working on CNTs. He was attempting to obtain few layer graphite using mechanical exfoliation method (see Figure 1.2(a)) [10]. While his "nano-pencil" method did not yield less than a few layers, the Geim group in Manchester found a simple method of obtaining single layer graphene in 2004(Figure 1.2(b)) [4]. Since then, there has been a mass

exodus of CNT scientists to its two dimensional cousin.

The reasons are obvious. For starters, many of the interesting electronic properties of CNTs are a subset of that of graphene. Secondly, many of the well established experimental techniques developed for 2-dimensional electron gas semiconductors (2DEG) could be simply be repeated on graphene. Despite the techniques themselves being antiquated, graphene is a material that substantially differs from conventional 2DEGs: it has a linear density of states and a linear energy dispersion relation, thus an effective mass of zero. Thirdly, the extraction method using mechanical exfoliation is very simple. A few hours of work can yield a significant amount of samples ready for lithographic patterning.

In just a few years, the progress on graphene has been remarkable. For example, it has been shown that by reducing the width of a graphene strip, the band gap can be controlled, effectively making it quasi-1D [11]. One can imagine a graphene wafer, patterned from a top down approach, with all the necessary components of a conventional electronic chip.

Still, complete abandonment of CNTs is premature because there is much science left to explore. Recent advancements like growth of centimeter long CNTs and top gating techniques open new avenues to address outstanding issues. CNTs still offer an outstanding material to do research on quantum dot and single-electron tunneling physics. Additionally, their 1D nature provides a structure to study Luttinger liquid physics.

1.3 Electronic Band Structure of Carbon Nanotubes

CNTs inherit their electronic band structure from graphene. Discussing the bonding of the carbon atoms that form graphene leads to its electronic properties, which can be obtained using the tight-binding or LCAO (linear combination of atomic orbitals) approach. We will see that this graphene is a semi-metal, or a zero-gap

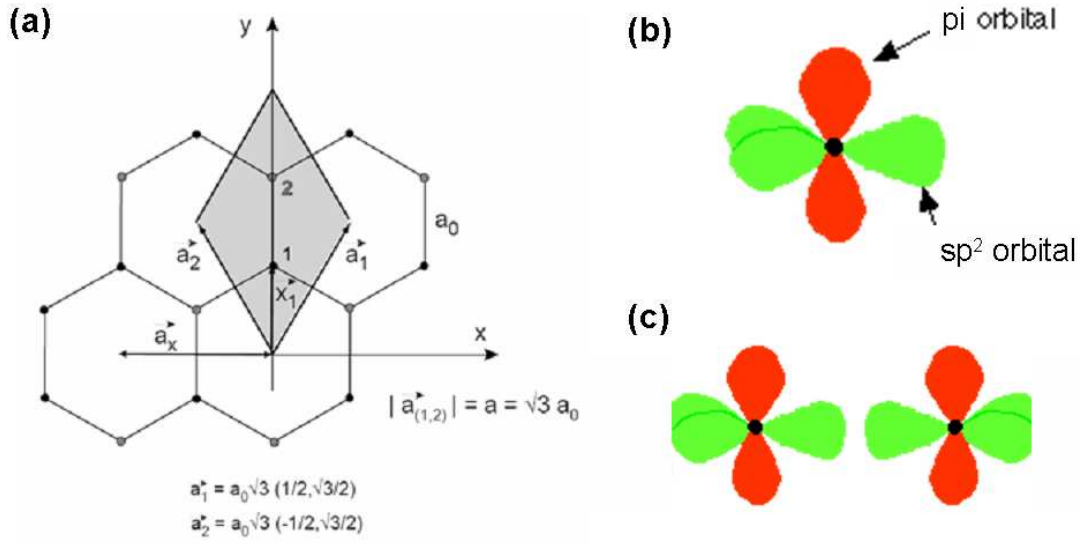

Figure 1.3: (a) Graphene is composed of a 2-dimensional array of carbon atoms arranged in a hexagonal lattice with a two atom basis (dark and light filled circles). (b) In crystalline form, the orbitals of the individual carbon atoms rehybridize to form three sp^2 orbitals 120° apart and one p_z orbital. (c) The sp^2 orbitals bond to its neighbors forming strong local covalent σ bonds, while the p_z orbitals form a continuous non-local π-band.

semiconductor, with a linear dispersion relation near the Fermi energy. By "wrapping up" a sheet of graphene the electronic band structure of CNTs can be obtained. Depending on the way the graphene sheet is wrapped, the CNTs are either metallic or semiconducting with an energy band gap inversely proportional to the cylindrical diameter.

Carbon is the sixth element of the periodic table and at the top of column IV. Each atom has 6 electrons in the configuration of: $1s^2 2s^2 2p^2$. The core electrons in the $1s^2$ shell are strongly bound to the nucleus, while the remaining valence electrons are weakly bound. In crystalline form, these valence electrons rehybridize to form more energetically favorably bonds with adjacent atoms. A specific type of rehybridization occurs in graphene, a sheet of carbon atoms arranged in a hexagonal lattice with a basis of two atoms (see Figure 1.3(a)). The valence electrons rehybridize into three sp^2 hybrids and a fourth p_z orbital (Figure 1.3(b)). The three sp^2 electrons each form σ-bonds in the x-y plane with its three neighbors 120° apart.

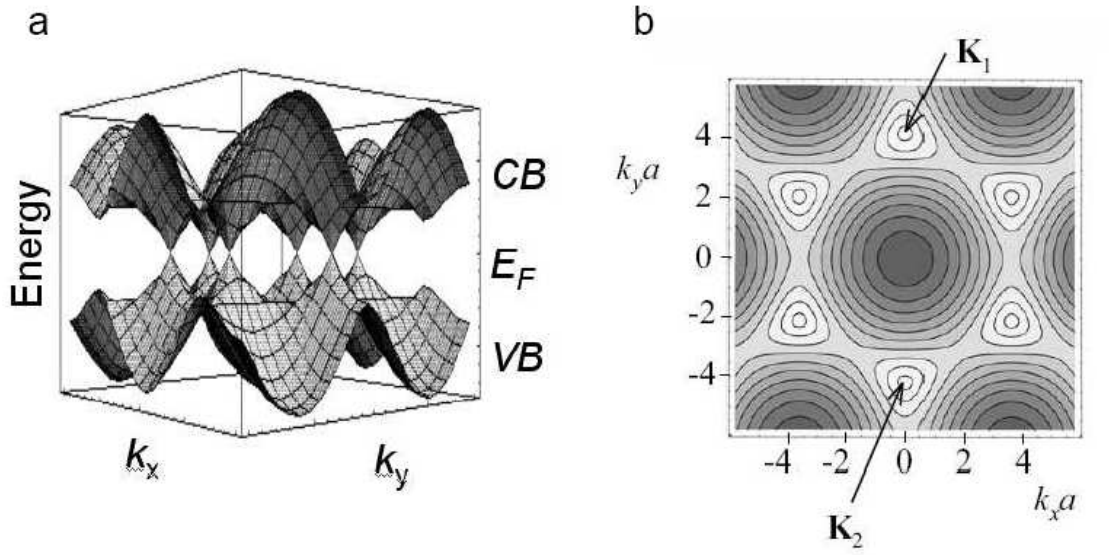

Figure 1.4: (a) Energy dispersion relation of graphene shows that the conduction band (CB) and valence band (VB) touch at the Fermi Energy. (b) Contour plot of the relation shows that these points form the corners of the hexagonal first Brillouin zone. The circles at these K-points reflect the conic structure of the band shape close to the Fermi Energy. The inequivalent K and K' points are a consequence of the real space lattice having a two atom basis. Adapted from Ref. [12].

The p_z electron remains orthogonal to that plane in the π-orbital (Figure 1.3(c)). The σ-bonds are local in nature; the electrons are strongly localized between the lattice of carbon atoms. When considering electron transport in graphene (and thus CNTs), we need to only consider the electron in the de-localized π-orbital. In contrast, it is the σ-bonds that are considered when discussing the cohesive structural properties of the material.

To determine the electronic characteristics of this network of atoms is a relatively straight forward solid state physics problem. In fact, P.R. Wallace completed this exercise using the tight-binding method as early as 1947 [13]. Instead of re-deriving the 2D energy dispersion relation here, I simply present the results as shown in Figure 1.4. At the Fermi energy, which is located at the six corners of the hexagonal Brillouin zone, the conduction and valence bands "touch" and the density of states vanishes. As a result of this feature, the material is called a zero-gap semiconductor or semi-metal. For small momentum k close to the Brillouin zone corner $K(K')$

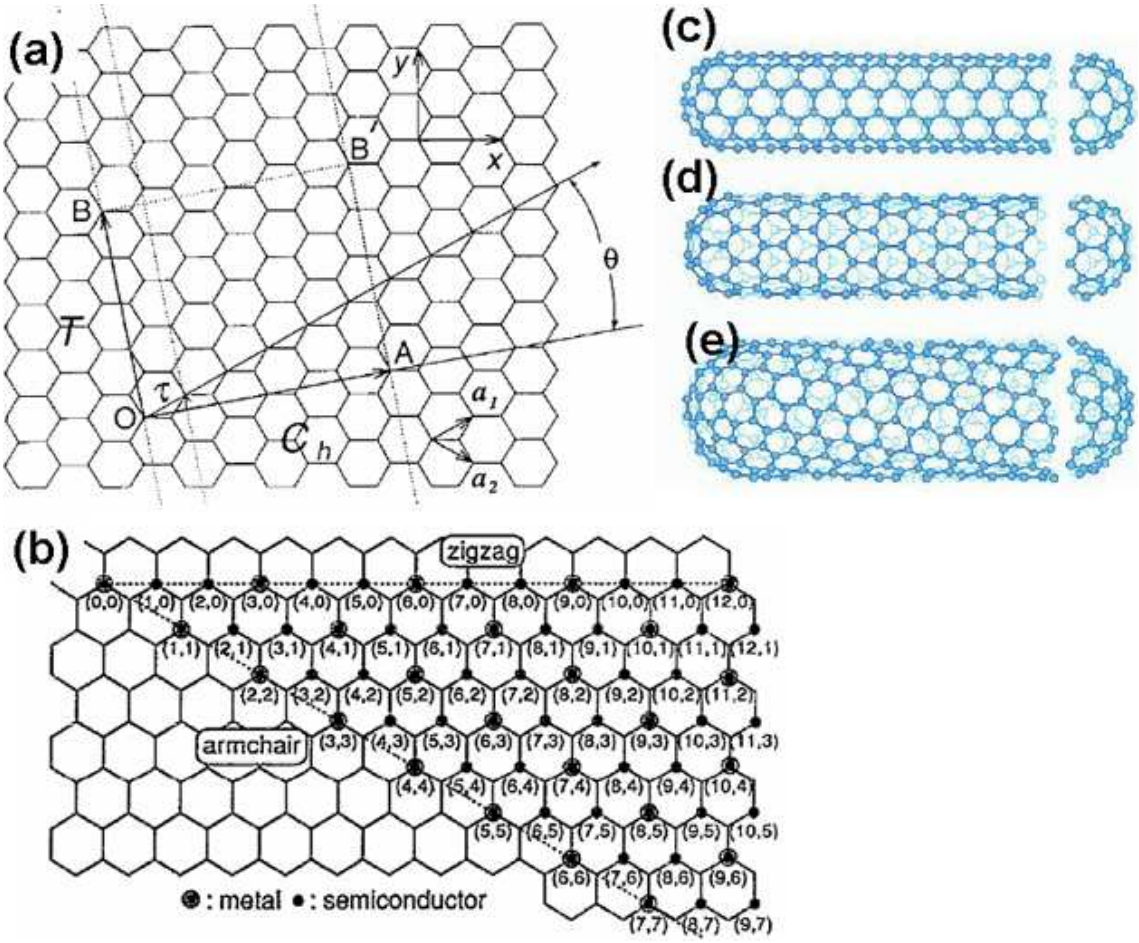

Figure 1.5: (a) The geometry of a carbon nanotubes can be conceptualized by wrapping graphene into a cylinder. The chiral vector $\vec{C_h}$ describes this wrapping and becomes the waist of the cylinder. (b) Indices (n,m) describe $\vec{C_h}$ and uniquely defines the CNT diameter and chirality. Three main types include: (c) armchair (n,m) with n=m, (d) zigzag (n,0) and (e) chiral (n,m) with n≠m. Adapted from Ref. [6]

the energy dispersion relation is given as $E = \hbar v_F k$, which in 2D represents a cone about the K point. Here, $\hbar$ is Planck's constant and v_F is the Fermi velocity.

By "wrapping up" a sheet of graphene, the CNT geometry can be conceptually formed as a seamless, hollow cylinder, although the are synthesized in a completely different manner. This conceptualization helps predict the CNT dispersion relation directly from the consideration of graphene. It is useful to define the chiral vector $\vec{C_h}$, which uniquely describes the variety of geometries possible for CNTs. Connecting the origin (0,0) or tail of vector $\vec{C_h}$ to its head (n,m) forms the CNT waist or equator

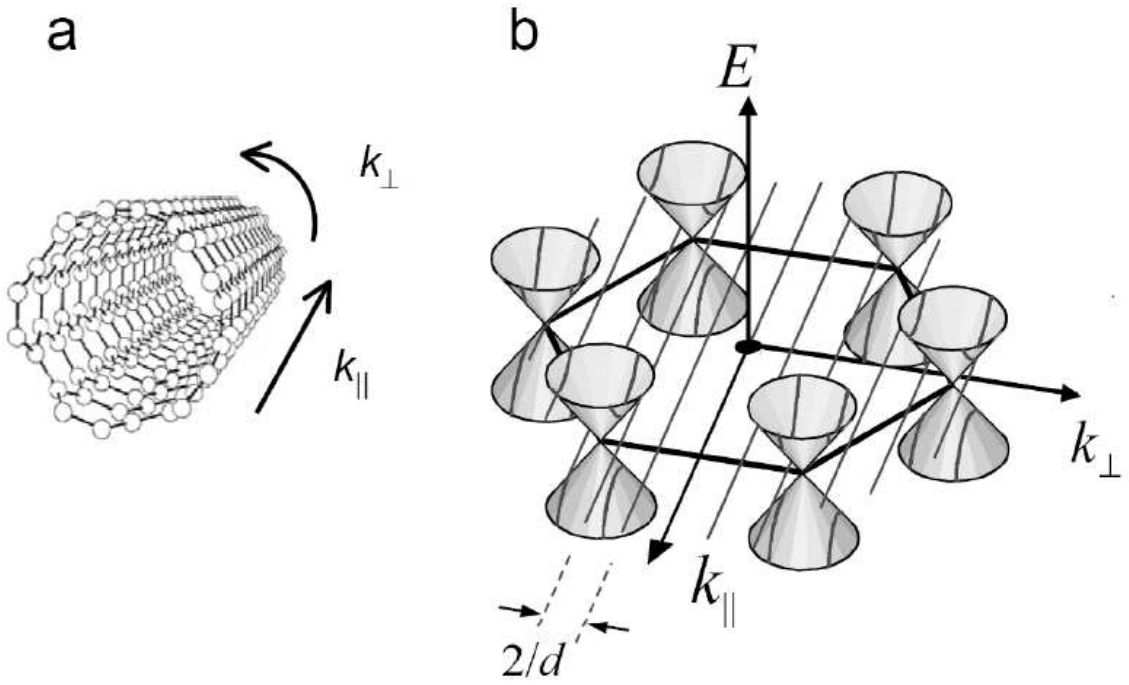

Figure 1.6: (a) The CNT equator, or circumferential direction perpendicular to the cylindrical axis, is typically on the order of a few nm's, while the direction parallel to the axis is on the order of microns. (b) The periodic boundary conditions in this direction impose restrictions on the $k_\perp$ of the 2D graphene dispersion relation. Depending on these restrictions, the CNT will be either metallic or semiconducting. Adapted from [12]

(see Fig 1.5(a)). The length of $\vec{C_h}$ divided by π defines the CNT diameter, while the angle $\vec{C_h}$ makes with the unit vector defines the CNT chirality. As a result of the hexagonal lattice symmetry, $0 < m < n$ are the only chiral vectors necessary to consider, as the rest are equivalent. Therefore, the indices (n,m) are a common, and unique, way to describe the CNT (see Fig 1.5(b)).

The single-walled carbon nanotube diameter d ranges from 0.7 to 4 nm. The length of $\vec{C_h}$ is typically much smaller than the length along cylindrical axis, which ranges from 100 nm to 10 cm (Figure 1.6). Therefore, the energy level spacing due to quantization in this direction is much larger. The quantization of the waveveector results from the application of periodic boundary conditions to $k_\perp$: $\vec{C_h} \cdot \vec{k} = \pi d k_\perp = 2\pi j$, where j is an integer. As a result, the 2D graphene dispersion relation is reduced to a series of 1D subbands superimposed on it.

This quantization results in arguably the most spectacular feature of CNTs. If the lowest 1D subband intersects the K point, the CNT will be metallic and if not, semiconducting. The separation of the subbands is inversely proportional to the diameter, so that the band gap, or twice the subbands' distance to the Fermi Energy, follows the same dependence (Fig. 1.6). In general, a tube defined as (n,m) will be metallic if n-m = 3q, where q is an integer and semiconducting if not.

1.4 A Brief Introduction into Electron Transport

Soon after the electron was discovered by J.J. Thompson in 1897, P. Drude was able to apply the kinetic theory of gases to metals to form a highly successful electron transport model. He surmised that a steady-state process takes place when an external electric field is applied across a conductor. The loosely bound electrons are accelerated in the direction of the field, while scattering of the electron sent it in the opposite direction. Incidentally, he did not need to specify the type of scattering mechanisms, only that it existed and occurred on average intervals. With these assumptions, he solved the classical Newton's Second Law of mechanics and found a linear relationship between the electric field and the current density, with a proportionality constant σ. From this picture, the average scattering time τ was able to be estimated from known parameters like electron mass and charge, along with measurable intrinsic material quantities, such as charge density and conductivity ($\tau = m\sigma/ne^2$). This linear relationship can be extended to reflect Ohm's Law. Drude's crude model is a rather remarkable achievement. However, this simple model breaks down when the conductor is larger than three characteristic length scales: the Fermi wavelength, the electron mean free path, and the phase coherence length, which are each discussed below.

(i) Fermi wavelength (λ_F) is the de Broglie wavelength of the electron. When the conductor is comparable to this length, the wave properties of the electron must be accounted for. In a neutral CNT, $\lambda_F = 2\pi/k_F = 3a_o = 0.75$ nm, independent of channel length. Hence, only in the circumferential direction where the CNT has

values on the order a nanometers is λ_F relevant. Considerations of the electron wave properties leads to quantization in this direction and ultimately to the 1D nature of CNTs.

(ii) Electron mean free path (L_m) is the average length an electron travels before a scattering event occurs. In a perfect crystalline lattice, electrons move freely through the lattice without any collisions. This simple picture breaks down, as there are deviations that destroy lattice symmetry that come from numerous sources such as phonons (lattice vibrations), impurities, defects, and environmental conditions (charge traps near the material). When the conductor is much larger than L_m the electron undergoes many collisions in the conduction channel, transport is diffusive and an averaging picture works well. When the channel length is on the order of L_m or less, transport is considered ballistic. Early theoretical work on CNTs before transport experiments were preformed predicted that L_m in CNTs would be anomalously long [14]. The work presented in this thesis experimentally confirms that at room temperature CNTs have an electron mean free path of ~ 1 μm, an order of magnitude greater than conventional 2DEGs [15], as well as other materials such as copper and silicon.

(iii) Phase coherence length (L_ϕ) is the length over which the electron maintains its phase information. This length can be longer than L_m, since elastic scattering preserves phase. When the relevant length scales are comparable to L_ϕ phase coherent transport occurs. For channel length L of a device with $L < L_m < L_\phi$, a Fabry-Perot-like resonance phenomena has been observed in CNTs [16]. When the channel length is very large, and $L_m < L_\phi < L$, the electron wavefunction becomes localized and Anderson localization has been observed [17].

As nanomaterials approach dimensions on the length scales described above, it is necessary to consider more complex descriptions of electron transport. For example, Ohm's Law suggests that as channel length tends towards zero the device resistance should also tend toward zero. Experimentally, it is found that when the conductor has a small number of conducting channels, the resistance tends noticeably towards a specific, finite value known as the quantum resistance. Furthermore, in mesoscopic

2DEGs, the resistance does not scale continuously linear with inverse width. Instead, the scaling of width introduces discreet modes that contribute to transport. The Landauer formula incorporates both of these attributes of smaller conductors in its formula for the conductance, G: $G = (2e^2/h)MT$, where M is the number of modes, and T is the transmission probability of the conductor. In the ballistic case of $T = 1$, the finite contact resistance is recovered. For large length scales, it can be shown that Ohm's Law is reproduced. For an excellent description of the Landauer formula, see Datta [18].

1.5 Fabrication

As a graduate student studying physics on the nanoscale, much time is devoted to device fabrication. While some device geometries are more difficult to fabricate than others, all CNT fabrication processes follow similar steps: (i) growth of carbon nanotubes on clean substrates (ii) lithography of alignment marks (iii) identifying CNT locations and performing atomic force microscopy to determine the CNT diameter (iv) device lithography (v) burning off excess CNTs on substrate (vi) dicing, bonding, and measurement. On paper, each individual step may seem trivial and easily reproducible. However, each step has the potential for failure of some sort (there is always a way!) and requires constant fine tuning to reflect the condition of the fabrication equipments.

Growth

The device geometries described in this thesis required long (>100 μm) CNTs. While there are multiple methods available to synthesize long CNTs, I exclusively used a method developed by a post-doc in our group, Byung-Hee Hong, who took a novel approach to the well-studied chemical vapor deposition (CVD) method. For a detailed explanation of CVD growth methods, please see Ref. [19]. In brief, $FeCl_3$ catalyst was applied to a Si/SiO_2 substrate, which was then loaded into a quartz

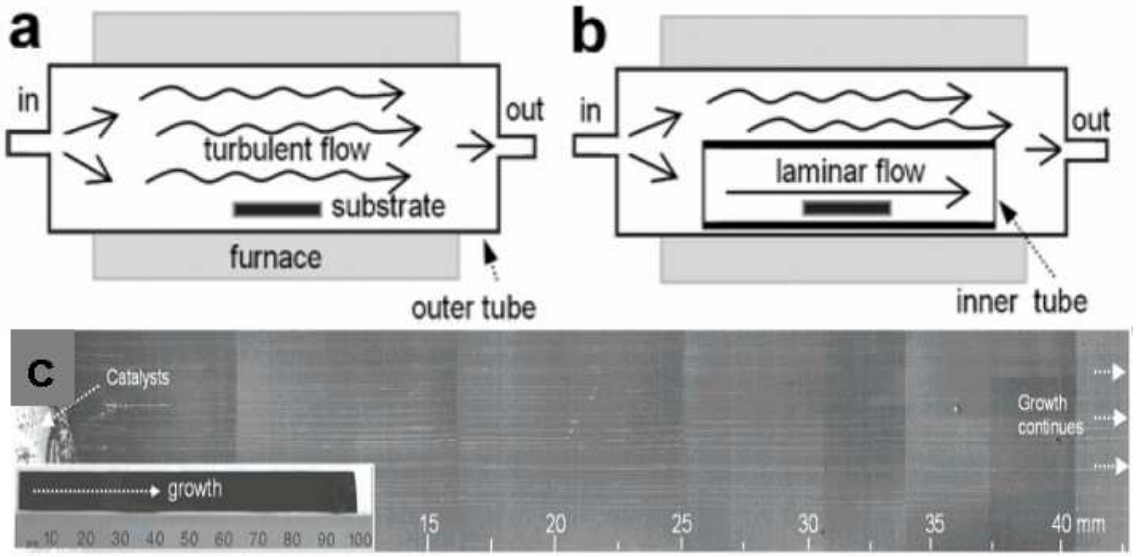

Figure 1.7: (a) Typical CVD method has methane gas flowing turbulently, resulting in curvy SWNTs that terminate with smaller lengths. (b) A smaller diameter quartz tube allows for laminar flow of methane gas and as a result, ultra-long SWNTs (c). Adapted from Ref. [5].

tube located in an oven. Once the temperature reaches $\approx 950°C$, methane gas is flowed through the quartz tube (Fig. 1.7a). Hong showed [5] that introducing a smaller, inner quartz tube allows for laminar flow of methane (Fig. 1.7b). The results were astonishing (Fig. 1.7c): SWNTs with a diameter of ≈ 2 nm and lengths that exceeded 10 cm - an aspect ratio of 10^8. To put this aspect ratio in perspective, if a human hair (which has a thickness of $\approx$100 μm) had the same ratio it would be 10 km long! That is enough to wrap around the "big loop" in Central Park, NYC. As far as we could tell, the length of the ultra-long SWNTs were only limited by the substrate and the oven size. This was the method we used to grow all our SWNTs. By changing the concentration of $FeCl_3$, the density of growth and CNT diameter could be controlled, as well as the ratio of single-walled to multi-walled CNTs.

Lithography: Alignment Markers

To build a device, it is necessary to determine the SWNT location. For this we use alignment markers, which are fabricated using electron beam lithography. We spin a layer of poly-methyl methacrylate, or PMMA onto the substrate and bake

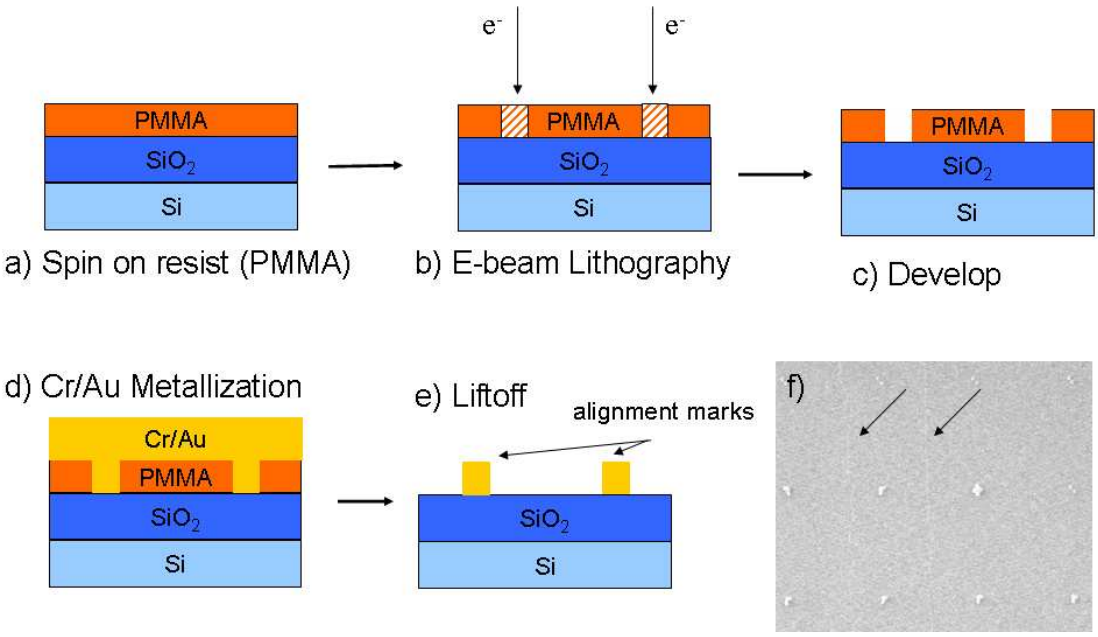

Figure 1.8: Typical fabrication process flow used to make samples discussed in this thesis. After CNT synthesis, it is necessary to fabricate alignment markers. This is done by (a) spinning PMMA on the substrate followed by using (b) electron beam lithography to design the markers. Afterwards, this is (c) developed, (d) metallized and then put in acetone overnight for (e) liftoff. A scanning electron microscope image shows our substrate with CNTs (arrows) and metal alignment markers. By specifying the location of the CNT relative to the alignment markers, devices can be fabricated using a similar fabrication process, but with a different pattern.

for 10 minutes at 180°C (Fig. 1.8a). We using a scanning electron microscope at 30 kV to "write" alignment markers randomly on the substrate (Fig. 1.8b). This is followed by development, where we immerse the substrate in a 3:1 mixture of isopropyl alcohol (IPA) and methyl isobutyl ketone (MIBK). The "written" areas of PMMA dissolve (Fig. 1.8c). Next, we metallize the entire chip (Fig. 1.8d) and then place it in a beaker of acetone overnight. The acetone dissolves the rest of the PMMA resulting in a "lift-off" of the metal that is not in contact with the substrate (Fig. 1.8e).

Image and Atomic Force Microscopy

Once there are alignment markers on the substrate, we can take an image of our sample with reference to the markers. Figure 1.8(f) shows a low-magnification, low-voltage scanning electron microscope image of the substrate after growth and alignment marker lithography. Two CNTs are visible and their locations relative to the alignment markers are well-determined. Sometimes, growth conditions shift so that single-walled and multiwalled carbon nanotubes grow on the same run. Before making contact to the CNTs, we AFM them to determine the diameter is less than 2.5 nm. While this does not screen multiwall CNTs with 100% certainty, it works well enough. Once the complete devices are fabricated, we probe the device electrically as another test.

Fabrication of Electrodes

Electron beam lithography of electrodes are similar to what is described above and displayed in Figure 1.8. However, in the case of electrode fabrication, the pattern design and metal used are both different. The design requires fine electrodes (1 μm) to contact to the CNT (Figure 1.9(c)) as well as macroscopic leads (100 μm) that can be wire bonded to for subsequent measurement. Typically, PMMA A5 is used in conjunction with scanning electron microscopy at 30 kV to perform electron beam lithography with dosages of 500 μC/cm^2. The finer patterns are written with spot size 1 ($I_{beam} = 25$ pA) and magnification 1200x, while the larger patterns are written with spot size 5 ($I_{beam} = 2500$ pA) and magnification 100x.

For transport experiments that measure the CNTs intrinsic characteristics, it is absolutely essential to obtain transparent contact to the CNTs, so that the electrode-CNT interface does not dominate transport. We found that palladium metal works best, which agrees with other experiments [20]. Using a thin (1 nm) adhesion layer of titanium helps the metal stick, but adds a resistance of 10 - 50 kΩ. On the other hand, we found that the chrome/gold hybrid adds 100 kΩ. In addition to choosing the proper metal for contact, it is necessary to avoid excessive exposure of the CNTs

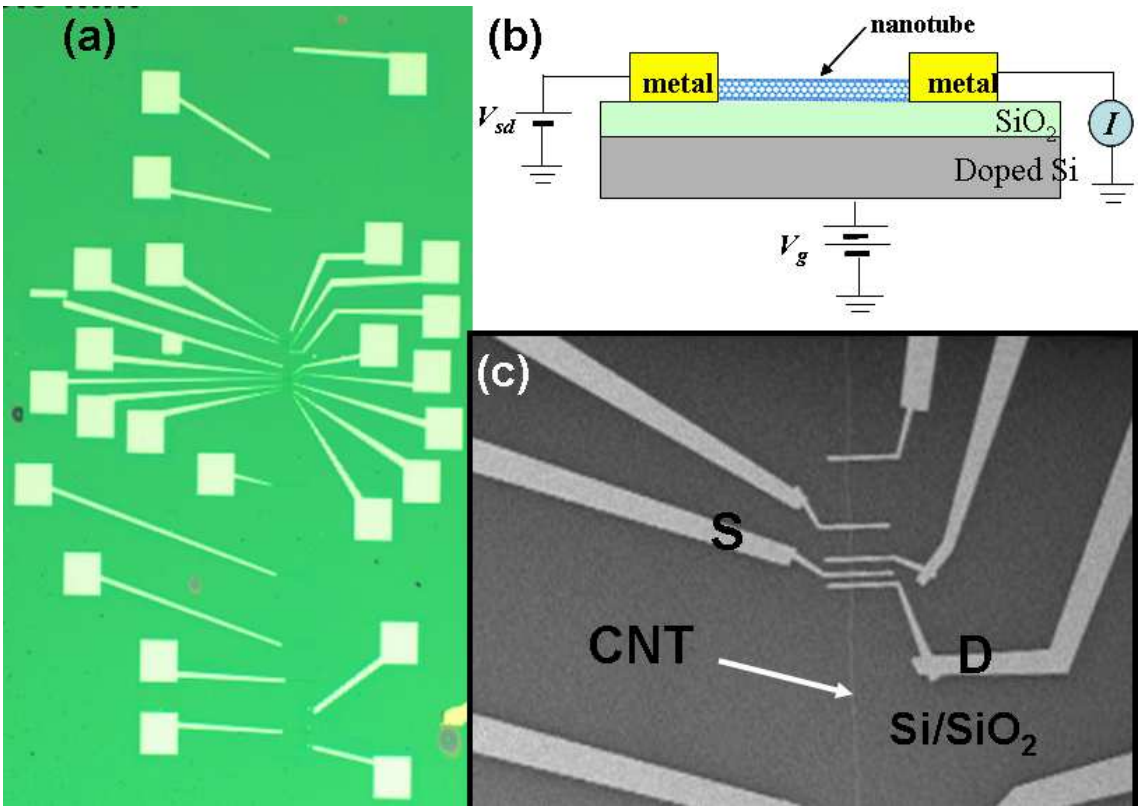

Figure 1.9: (a) Optical microscope image of a typical device. The large pads will be wirebonded into a ceramic chip holder so that it can be measured at low temperatures in a cryostat. (b) A schematic of the the real device (c). Typically, a small DC voltage is applied to the source (S) and the DC current is measured from the drain (D), while the Si/SiO_2 substrate serves as a global back gate electrode.

to invasive imaging, such as scanning electron microscopy at 1 kV. It may result in the deposition of unwanted carbon soot and create additional contact resistance. This is one benefit of the ultra-long growth: the CNTs can be imaged at relatively low magnification to obtain its position relative to the alignment markers.

Packaging and Measurement

If possible, we fabricate an extra two-terminal device away from the desired sample, but on the same CNT. On this expendable device, we do an electrical high-bias test where we use a large source-drain bias and measure current, which should saturate

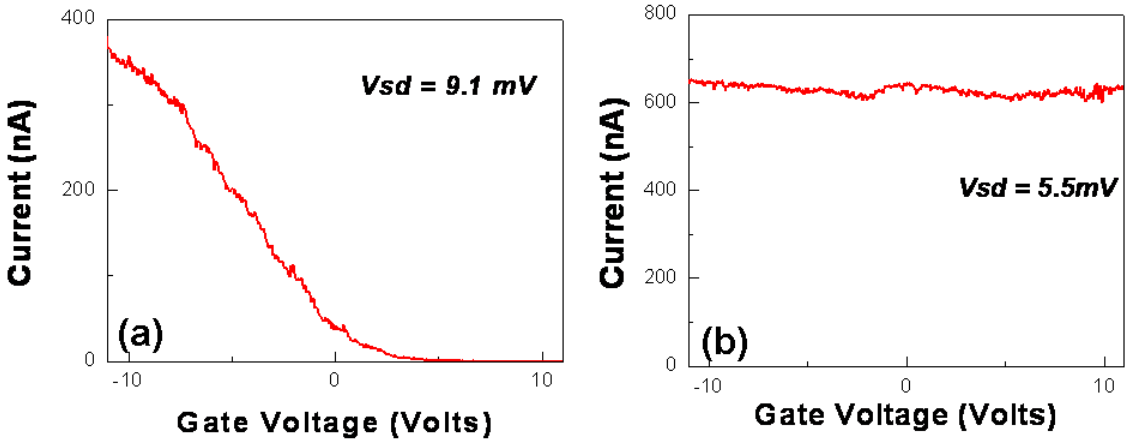

Figure 1.10: With the source-drain voltage fixed, the back gate voltage can be tuned to reflect (a) a semiconducting CNT, where the current becomes small when the Fermi energy lies in the energy band gap or (b) a metallic CNT, where the current is independent Fermi energy.

to ≈ 25 μA for single-walls, reflecting the 4 conducting channels [7]. We do this on an expendable device because the high bias may incur some damage to the CNT or the CNT-electrode interface. With this process, we confirm that the CNT is single-walled, beyond AFM measurement of the diameter.

Before we can measure the completely fabricated device, we must dice the substrate and glue it into a "chip holder", which we can make macroscopic bonds to. This allows us to secure the device in a cryostat, where we can measure the sample at various temperatures. We highlight some important ways to electrically probe it to learn about its transport properties. First, in a two-terminal setup, a small DC voltage is applied to a "source" contact and the current going through the device is measured from the "drain" contact. This allows for measurement of an IV curve and provides information of the device resistance. Secondly, it is possible to control the Fermi energy in the CNT because it is capacitively coupled to the substrate. By applying a "gate" voltage V_g to the degenerately doped silicon, the charge in the CNT is changed and effectively tunes the Fermi energy E_F. For fixed V_{SD}, the current can be measured as a function of V_g, which is roughly the same as tuning E_F (Figure 1.10).

The capacitance of a CNT is described in Ref. [21]. Briefly, there are two main

components to the capacitance of the CNT. The classical component is strictly based on the geometry. The geometrical capacitance of a CNT on substrate is well described by approximating it as a cylinder on a two-dimension plane: $C = 2\pi\varepsilon L/\ln(4h/d)$, where $\varepsilon = 3.9\varepsilon_o$ for SiO_2, h is the separation, and d is the diameter. The other main component to the total capacitance is related to the density of states. As the Fermi energy is shift, it requires additional energy to add electrons.

By tuning V_g, it is possible to measure the transport properties from deep in the valence band to deep in the conduction band. This is one way to tell if the CNT is semiconducting (V_g dependence as in Fig. 1.10(a)) or metallic (no V_g dependence as in Fig. 1.10(b)). In the case of semiconducting CNTs, an additional factor in transport is the Schottky barrier. Since the CNT is typically p-doped, device properties in the valence band (negative V_g values) are easier to measure. Finally, a way to extract rich transport information about the CNT is the stability diagram. To perform this measurement an IV curve is taken for a fixed value of V_g. Subsequently, V_g is stepped and the process is repeated. In this way, it is possible to extract the size of the band gap and see how transport properties are effected for various values of E_F.

Chapter 2

Electron Mean Free Path in Single-Walled Carbon Nanotubes

2.1 Introduction

Background

The mean free path is the distance an electron traverses before it scatters. In this chapter, we report on the electron mean free path (L_m) in single-walled carbon nanotubes (SWNTs) [8]. It is a fundamental length scale because of the role it plays in determining a conductor's transport regime. Its magnitude relative to the phase coherence, localization, and channel lengths determine the transport phenomena observed: (i) diffusive or ballistic conduction [22, 23, 16, 24, 20], (ii) strong localization [17], or (iii) co-tunneling and variable range hopping [25]. These regimes have been observed in SWNTs despite the lack of a comprehensive and explicit determination of L_m in SWNTs over a range of temperatures, which is the focus of this work.

Previous Estimations and Experiments

In a limited fashion, the mean free path in SWNTs has been measured in a variety of ways. One method to estimate L_m is to observe ballistic conduction. This is an indication that the electron has traversed the conduction channel without the occurrence of a scattering event. In a ballistic SWNT, the device resistance approaches $R_q = (h/4e^2)$ without an explicit dependence on the channel length L. Here, the factor 4 reflects the 2 independent conduction channels for spin and 2 for the band degeneracy [6]. This method determines a lower limit for L_m: $L_m > L$. Experiments of this kind at low temperature and low bias yield estimates of: (i) $L_m > 200$ nm [16], (ii) $L_m > 500$ nm [24], and (iii) $L_m > 4$ μm [20]. At higher bias (>0.16 eV), where temperature does not matter since 300 K $\sim$ 26 meV, an L_m >15 nm was estimated [22]. This method produces an order of magnitude estimate of L_m and only gives a lower bound instead of a precise value. Furthermore, this method works only at lower temperatures for low bias, so it does not provide any information on temperature dependence.

An alternative method to experimentally determine L_m uses non-invasive probes to obtain the four-point resistance and effectively eliminate contact resistance [26]. At lower temperature, however, quantum interference leads to a measurement of negative resistance, so L_m is often not well defined where the phase coherence L_ϕ becomes longer than the channel length ($L < L_\phi$). Another experimental approach uses scanning probe microscopy to measure the linear scaling of the resistance [27]. Unfortunately, due to experimental limitations imposed by their scanning probe setup, only room temperature values were measured. Both of these exciting experiments estimated L_m to be on the order of 100 nm for T= 300 K.

Our Approach

Our experimental method allowed us to obtain well-defined values of L_m for a range of temperatures on the same SWNT. This is in contrast to the vague low temperature estimates in the works described above. This experiment also fills the void of L_m

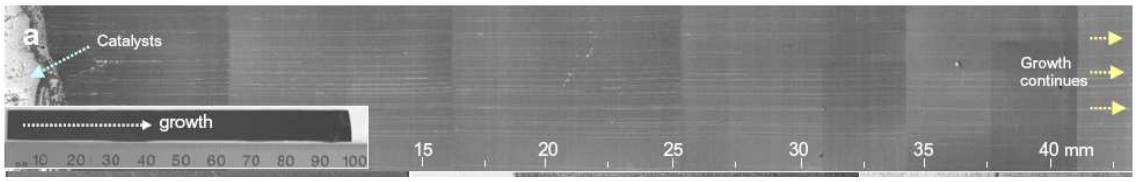

Figure 2.1: A scanning electron microscope image of a SWNT from Ref. [5]. The inset shows SWNTs spanning the entire chip (10 cm). As far as we can tell, the fundamental limitation to length we can grow the SWNT is imposed by the size of the substrate and the CVD oven it is grown in.

estimates between low temperature ($T \sim 1.6$ K) and room temperature. The recent advances in the growth of extremely long SWNTs (>1 mm), particularly in our lab [5] (see Fig. 2.1), has allowed for an intensive study of their intrinsic properties. In this Chapter, I present experimental measurements on the scaling behavior of resistance in individual, millimeter long SWNTs for the temperature range of 1.6 - 300 K. From the linear scaling of resistance, the temperature dependent electron mean free path is calculated for each temperature. In Chapter 3, I will discuss results beyond the linear scaling regime, where we observe that the resistance increases exponentially with length.

2.2 Fabrication of Multi-Electrode SWNT Devices

Macroscopically long and straight individual SWNTs were grown on a degenerately doped Si/SiO_2 substrate ($t_{ox} = 500$ nm) using the chemical vapor deposition method described in Ref. [5] and the previous chapter. This was followed by the fabrication of multiple palladium (Pd) electrodes with various separations (200 nm - 400 μm) (Fig.2.2(a)). Pd electrodes were chosen to create highly transparent SWNT-electrode contact [20]. The diameters of the SWNTs were measured by atomic force microscope (AFM). We chose SWNTs with diameter d less than 2.5 nm to exclude any possibility of including multiwalled nanotubes (MWNT) in this study. In addition, we confirmed that the high bias saturation current is < 30 μA for all SWNTs studied, assuring that the samples consisted of single SWNTs rather

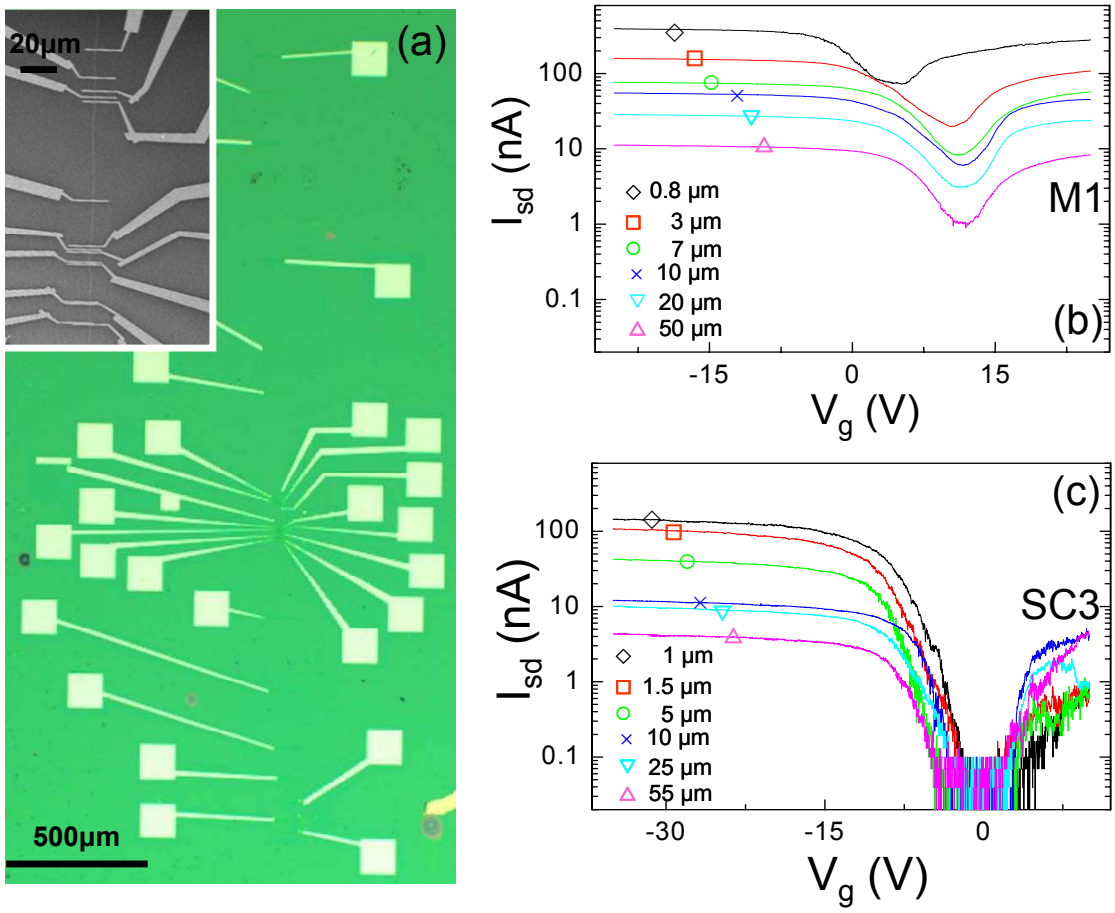

Figure 2.2: (a) Optical image showing typical SWNT devices with multiple Pd electrodes. (Inset) Scanning electron microscope image of an isolated SWNT contacted with these electrodes. Room temperature $I_{SD}(V_g)$ of selected channel lengths for (b) metallic SWNT (M1) and (c) semiconducting SWNT (SC3) with $V_{SD} = 6.4$ and 2.7 mV, respectively.

than small bundles or MWNTs [7].

2.3 Measurement Methods

Conductance Curves

The substrate was used as a gate electrode to tune the chemical potential of the sample by the application of a gate voltage (V_g). A small dc source-drain bias voltage ($V_{SD} < 10$ mV) was applied between pairs of consecutive electrodes and

the two-terminal linear response conductance was determined from the measured source-drain current I_{SD}. Fig. 2.2 (b-c) shows the measured I_{SD} as a function of V_g for selected channel length sections on two representative SWNTs.

All curves exhibit a "gap" like feature - a range of V_g where I_{SD} is suppressed. On the same SWNT, every device (pair of consecutive electrodes) shows a similar $I_{SD}(V_g)$ up to a length-dependent multiplicative factor, once we align the centers of the gap region for each curve. The similarity of the $I_{SD}(V_g)$ behavior in different sections for each SWNT sample indicates that the corresponding "gap" features are derived from the intrinsic electronic structure of the SWNT rather than the effects of random local variation. For approximately 3 out of 50 samples measured we observed the $I_{SD}(V_g)$ behavior change in various sections of the same sample over a length scale of a few millimeters, i.e. changing from a small gap to a large gap. The change was discrete, implying that there may have been an abrupt variation in chirality during the growth. We did not use these samples in our analysis.

Metallic and Semiconducting SWNTs

We use the qualitatively different $I_{SD}(V_g)$ behaviors of different SWNTs to categorize them as metallic (M-NT) or semiconducting nanotubes (S-NT). Typical S-NTs (Fig. 2.2(c)) exhibit an off current region of $I_{SD} < 10^{-10}$A when the Fermi energy E_F lies in the energy band gap [28, 9]. On the other hand, a weaker suppression of $I_{SD}(V_g)$ is observed in the "small gap" region in M-NTs (Fig. 2.2(b)). The 'small gap' in M-NTs has been attributed to the curvature-induced energy band gap E_g <100 meV [29], which is distinguished from the S-NT energy band gap, which scales with diameter as $E_g \sim 450$ eV$/d$ [nm] [6].

The size of the smaller energy gap can be experimentally determined at lower temperatures. We characterize the M-NT in Fig. 2.2(b) at 1.6 K using a stability diagram, or 3-dimensional plot (Fig. 2.3). The differential conductance dI/dV is plotted as a function of V_{SD} (vertical axis) and V_g (horizontal axis). We plot log(dI/dV) to distinguish the lower conducting regions (dark scale) from the higher

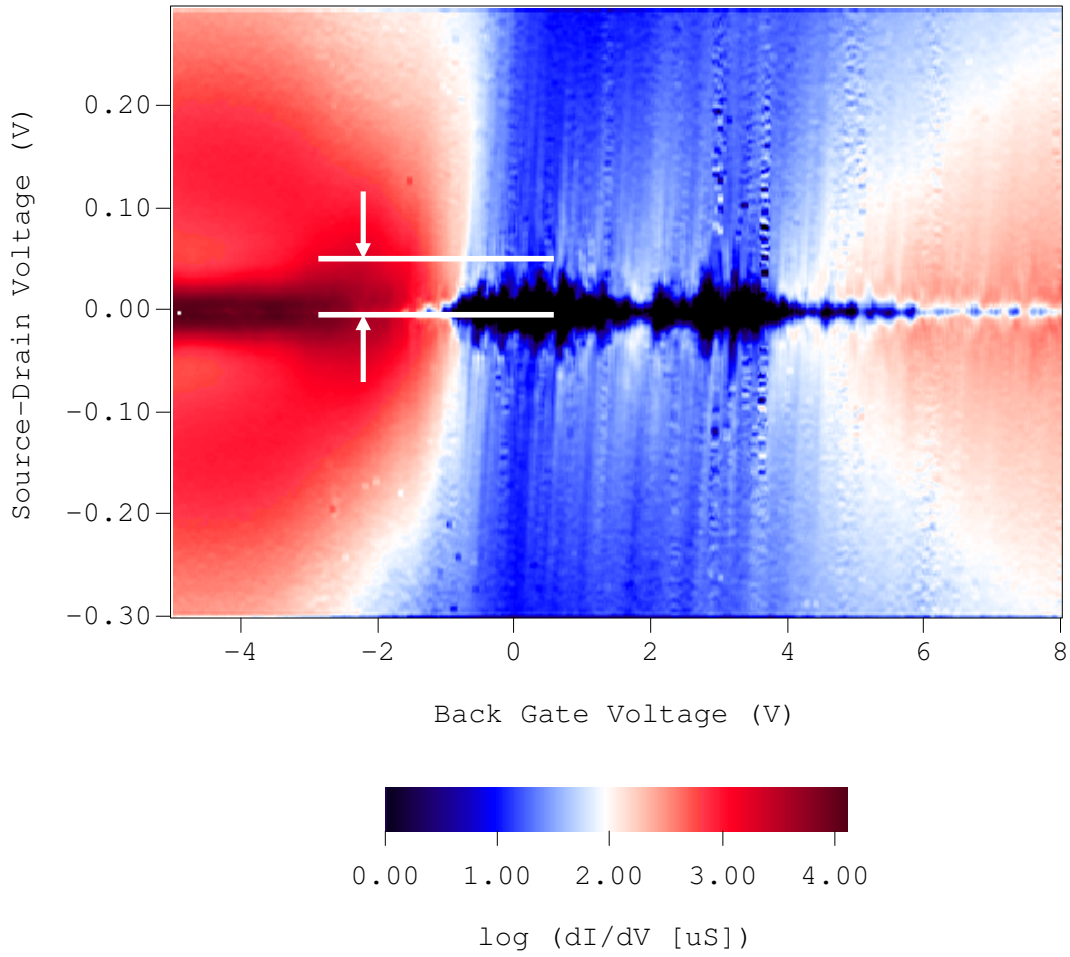

Figure 2.3: Stability diagram for the M-NT sample in Fig. 2.2 (b) at 1.6 K and $L = 5$ μm. The logarithm of the differential conductance is plotted to highlight lower conductance regions (dark scale) from the higher conductance regions (lighter scale). An energy gap of 40 meV can be read directly from the diagram (white arrows).

conducting regions (lighter scale). The benefit of plotting the data this way is that the energy band gap can be read directly off the diagram: the white arrows indicate $E_g \approx 40$ meV. This is consistent with the energy scale of a curvature induced gap on a M-NT [30]. Among the 11 SWNTs we studied in this letter, we found 4 M-NTs and 7 S-NTs. Each of these SWNTs exhibit a gap centered at $V_g > 0$, indicating their p-doped nature.

2-Terminal Measurements in SWNTs

At large negative gate voltage (V_g <-20V), E_F lies well outside of the energy band gap region and $I_{SD}(V_g)$ saturates to I_{SD}^{sat} (Fig. 2.2(b) and (c)), whose value depends only on the applied V_{SD} and channel length L of the SWNT section. The two-terminal resistance of the SWNT section is then obtained from $R(L) = V_{SD}/I_{SD}^{sat}$. When E_F lies well outside the gap region in a 1D SWNT the energy dispersion relation is linear so that the density of states and Fermi velocity is constant. Thus, a saturated $I_{SD}(V_g)$ implies that the scattering time τ and mean free path is independent of E_F in this regime.

Four-terminal resistance (R_{4t}) measurements are possible for each section by utilizing the available multiple electrode configuration. However, in our experiment, four terminal measurements yield similar results to the two terminal resistance (R_{2t}) (Fig. 2.4). In general, contact resistance is a significant obstacle when dealing with transport measurements in SWNTs. Inseparable contact resistance of the SWNT and metal electrodes interface was reported to be caused by the invasiveness of metal contacts [31]. Electrons traveling from the outer electrodes are inelastically scattered by the inner voltage terminals, which is precisely why they are considered invasive. These scattering events equilibrate the local chemical potential around the electrode and effectively segments the tube. As a result, R_{4t} is roughly equal to R_{2t}. Indeed, Makavorski et al. estimated that only 10% of the electrons maintain their initial chemical potential after passing an electrode probe [32]. In our own experiment, we show the negligible differences between 4-terminal and 2-terminal measurements at different V_g in Fig. 2.4. Generally, the difference between R_{4t} and R_{2t} becomes negligible as V_g moves away from the band gap, where the interfacial Schottky barrier becomes transparent.

By considering the scaling of $R(L)$, the contact resistance contribution can be estimated and thus removed from our analysis. This attribute of our experiment is one of the aspects that make it appealing. We are able to extricate which part of

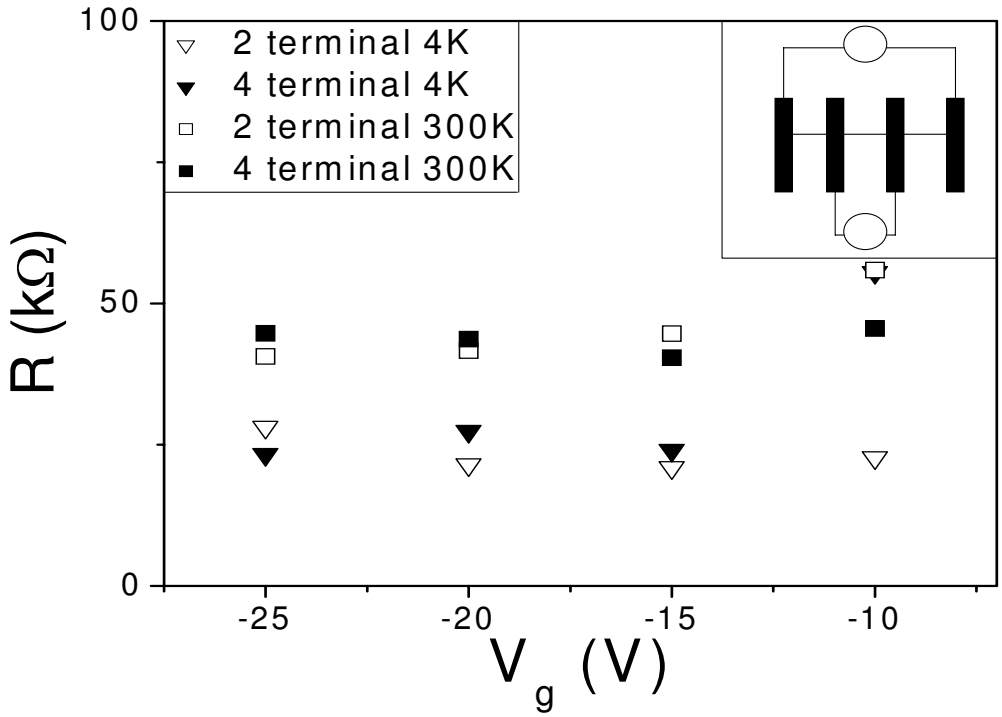

Figure 2.4: (Inset) Resistance can be measured in a 4-terminal geometry, where a current is supplied from the outside electrodes and a voltage is measured by the inside electrodes or a 2-terminal measurement where V_{SD} is applied to one electrode and I_{SD} is measured from the next consecutive one. (Main) In many mesoscopic structures, 4-terminal measurements are a way to eliminate contact resistance, but not in a 1-D SWNT. The difference in the resistance is negligible because the electrodes themselves are invasive.

the measurements are intrinsic to the SWNT and determine contact related contributions separately.

2.4 Linear Scaling of Resistance

Scaling of Resistance

We designed many pairs of electrodes with channel lengths spanning 4 orders of magnitude on each SWNT so that the scaling of $R(L)$ can be studied for a specific

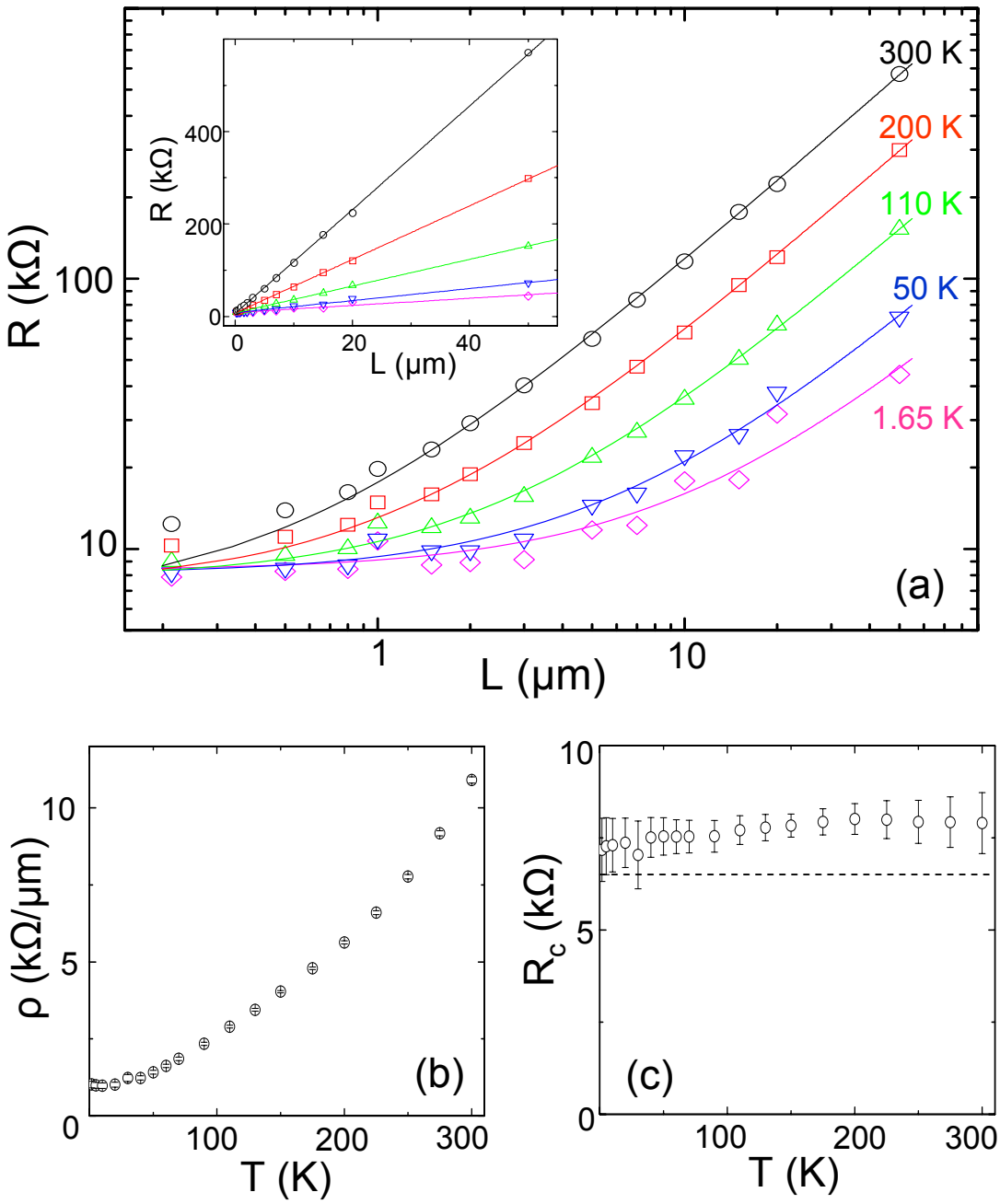

Figure 2.5: (a) (Inset) $R(L)$ for sample M1 at select temperatures ranging from 1.6 - 300 K. (Main) A log-log plot highlights the behaviors at different lengths scaling 3 orders of magnitude. From the linear fits (solid lines) of these data points, we obtain the 1D resistivity (b) and the contact resistance (c) at different temperatures. The dashed line in (c) represents R_Q.

sample at a given temperature T. Figure 2.5(a) shows $R(L)$ of a representative SWNT measured in the temperature range of 1.6 - 300 K and with a channel length range of 200 nm - 50 μm. In these ranges, $R(L)$ increases linearly and appears to converge to a finite value for small L . This scaling behavior can be described well by a simple linear dependence with an offset: $R(L) = \rho L + R_c$, where ρ and R_c are interpreted as the 1D resistivity and contact resistance, respectively. The solid lines in Fig. 2.5(a) are the two parameter line fits of the data points at a given T value. From these fits, $R_c(T)$ and $\rho(T)$ are obtained as shown in Fig. 2.5(b) and Fig. 2.5(c), respectively. For this sample, R_c remains fairly constant at $\sim$8 $k\Omega$ and $\rho(T)$ exhibits typical metallic behavior, i.e. it decreases with T and saturates to a value ρ_{sat} at low temperatures. Similar scaling behavior of $R(L)$ is observed in other SWNTs, from which both R_c and $\rho(T)$ are extracted within the linear scaling regime. Table 2.1 and Table 2.2 summarizes d, R_c, and ρ_{sat} for the 4 M-NTs and 7 S-NTs considered in this study.

To understand the scaling of $R(L)$ in Fig. 2.5 we begin with the two-terminal Landauer-Buttiker formula applied to SWNTs [27]. If we consider 4 low-energy channels in the SWNT, 2 each for spin and band degeneracy, then the scaling of resistance is given by $R(L) = (h/4e^2)(L/L_m + 1) + R_{nc}$, where e and h are electron charge and Plank's constant and L_m and R_{nc} are the electron mean free path and the non-transparent contact resistance, respectively. Note that we separate out the contribution of R_{nc} from the total contact resistance R_c, so that the contact resistance becomes the quantum resistance $R_Q = h/4e^2$ when the contacts become fully transparent.

Table 2.1: Device characteristics for metallic SWNTs used in this study.

	M1	M2	M3	M4
$d(nm)$	$2.0 \pm .2$	$1.3 \pm .4$	$1.7 \pm .6$	$1.6 \pm .4$
$R_c(k\Omega)$	$7.9 \pm .8$	11.5 ± 2.9	8.3 ± 2.5	12.0 ± 4.4
$\rho_{sat}(k\Omega/\mu\text{m})$	$0.76 \pm .02$	$0.87 \pm .02$	$0.93 \pm .01$	$6.5 \pm .08$
$L_m^{sat}(\mu\text{m})$	$8.56 \pm .23$	$7.65 \pm .17$	$7.07 \pm .08$	$1.00 \pm .01$

Table 2.2: Device characteristics for semiconducting SWNTs used in this study.

	SC1	SC2	SC3	SC4	SC5	SC6	SC7
$d(nm)$	$1.6 \pm .4$	$1.8 \pm .6$	$1.9 \pm .4$	$2.1 \pm .2$	$2.2 \pm .2$	$2.0 \pm .6$	$2.2 \pm .2$
$R_c(k\Omega)$	10.2 ± 4.5	14.9 ± 5.7	$10.4 \pm .9$	7.0 ± 2.3	25.4 ± 4.2	6.9 ± 40	21.8 ± 14
$\rho_{sat}(k\Omega/\mu\text{m})$	$2.95 \pm .05$	$3.61 \pm .05$	$4.64 \pm .01$	$5.91 \pm .12$	$8.13 \pm .31$	$14.1 \pm .19$	$16.3 \pm .13$
$L_m^{sat}(\mu\text{m})$	$2.24 \pm .04$	$1.83 \pm .03$	$1.40 \pm .01$	$1.10 \pm .02$	$0.80 \pm .03$	$0.47 \pm .01$	$0.40 \pm .01$

Resistance versus Channel Length & Temperature

From the experimentally obtained data, we explore the resistance of SWNTs in a 2 parameter phase space: resistance as a function of L and T. In Figure 2.6, we show this in a 3-dimensional plot for representative metallic and semiconducting SWNTs, which each show distinct behavior. For example, the resistance of the metallic sample decreases with temperature for all channel lengths (Fig. 2.6 upper right) and it also scales linearly with length. In contrast, the resistance of the semiconducting sample SC3 (Fig. 2.6 upper left) decreases with temperature only until a critical value T^*. Below T^*, which has higher values for longer channel lengths, the resistance does not scale linear with length. In some semiconducting devices, this increase in resistance at lower temperatures is much more pronounced, as in sample SC6 (Fig. 2.6). For all samples, however, at higher temperatures and shorter channel lengths, the scaling is linear and will be the focus of this chapter. In the next chapter, we will discuss the regime where the scaling is non-linear.

Determining Linear Regime

It is clear from Figure 2.6 that at lower temperatures and longer channel lengths the SWNT resistance does not scale linear with length. In order to determine the temperature ranges and length scales for linear scaling analysis, we use the following

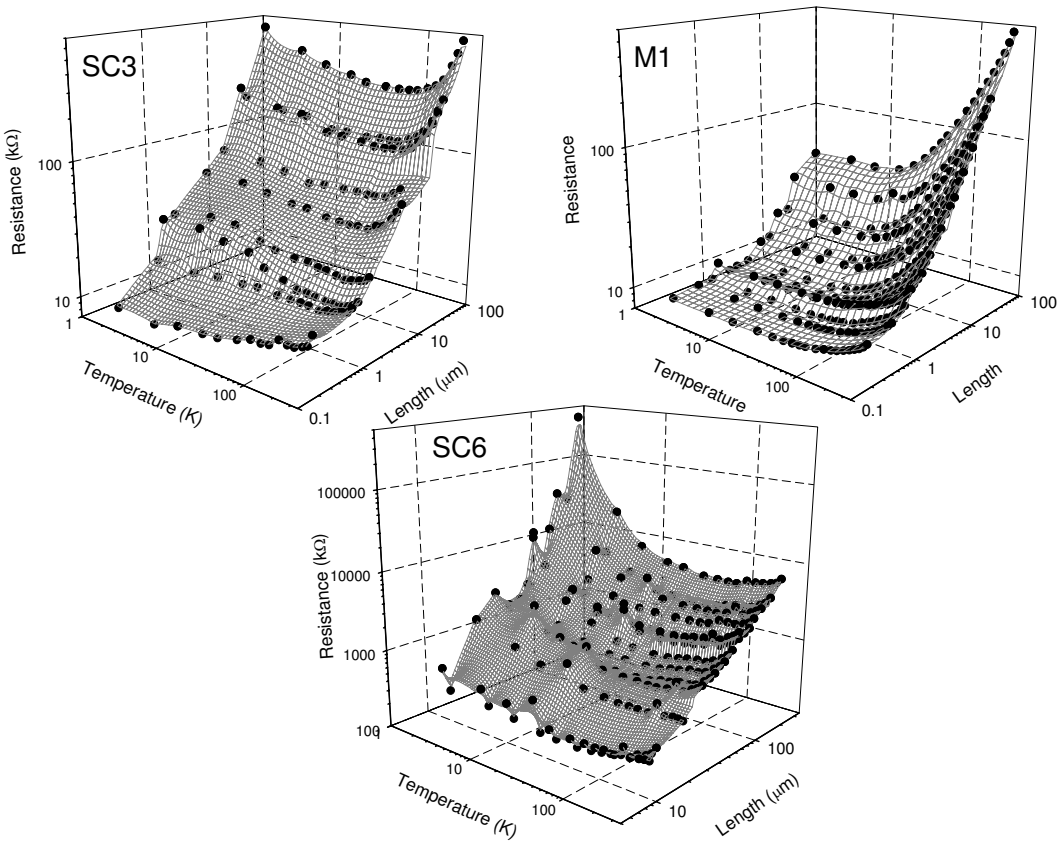

Figure 2.6: A 3-dimensional plot of device resistance as a function of T and L for 3 different SWNTs: (clockwise from upper right) M1, SC6, and SC3.

phenomenological criterion. First, we observe the temperature dependence of the resistance for a device of fixed channel length (Fig. 2.7). The resistance decreases with T until it reaches a length dependent T^*. All data points with $T > T^*$ are included in the linear scaling analysis. Since metallic behavior (i.e. $\mathrm{d}R/\mathrm{d}T > 0$) is well correlated to the linear scaling of $R(L)$, this criterion works well to study the resistivity of SWNTs. Data points for $T < T^*$ are analyzed in the next chapter, where we consider non-linear effects. Although the resolution is limited to ± 20 K because of the lack of temperature data points, in general T^* decreases with channel length.

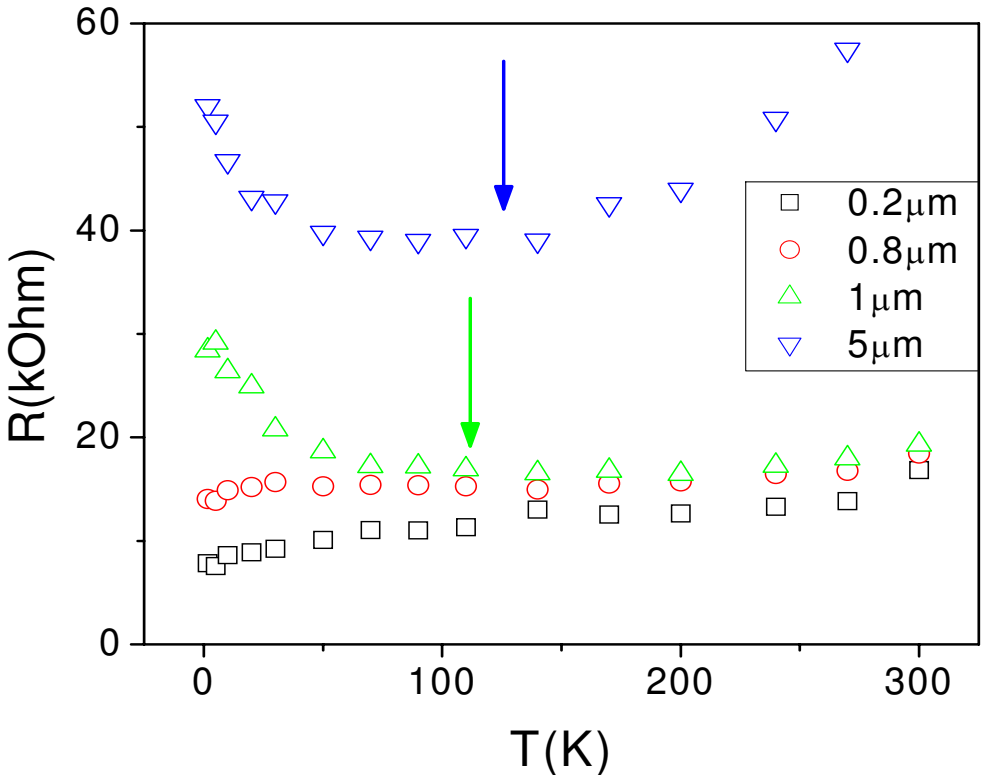

Figure 2.7: R versus T for devices with different L on the same SWNT. The general trend observed is that the resistance decreases with temperature until a length dependent T^* (indicated by arrows). For the linear scaling analysis, only data points for $T > T^*$ are included.

2.5 Mean Free Path in SWNTs

From $\rho(T)$ to $L_m(T)$

From the experimentally obtained $\rho(T)$ and R_c, we can deduce $L_m = R_Q/\rho(T)$ and $R_{nc} = R_c - R_Q$ for each of our SWNT samples. In particular, we note that $R_{nc} \leq R_Q$ for the majority of our samples, suggesting that the barrier at the contacts is very thin and adds only a negligible contribution when L becomes substantially large. We now discuss the temperature dependent behavior of the electron mean free path. Figure 2.8 is the central result of this chapter, showing $L_m(T)$ for the SWNTs listed in Table 2.1. Each color represents a different SWNT; open circles are the

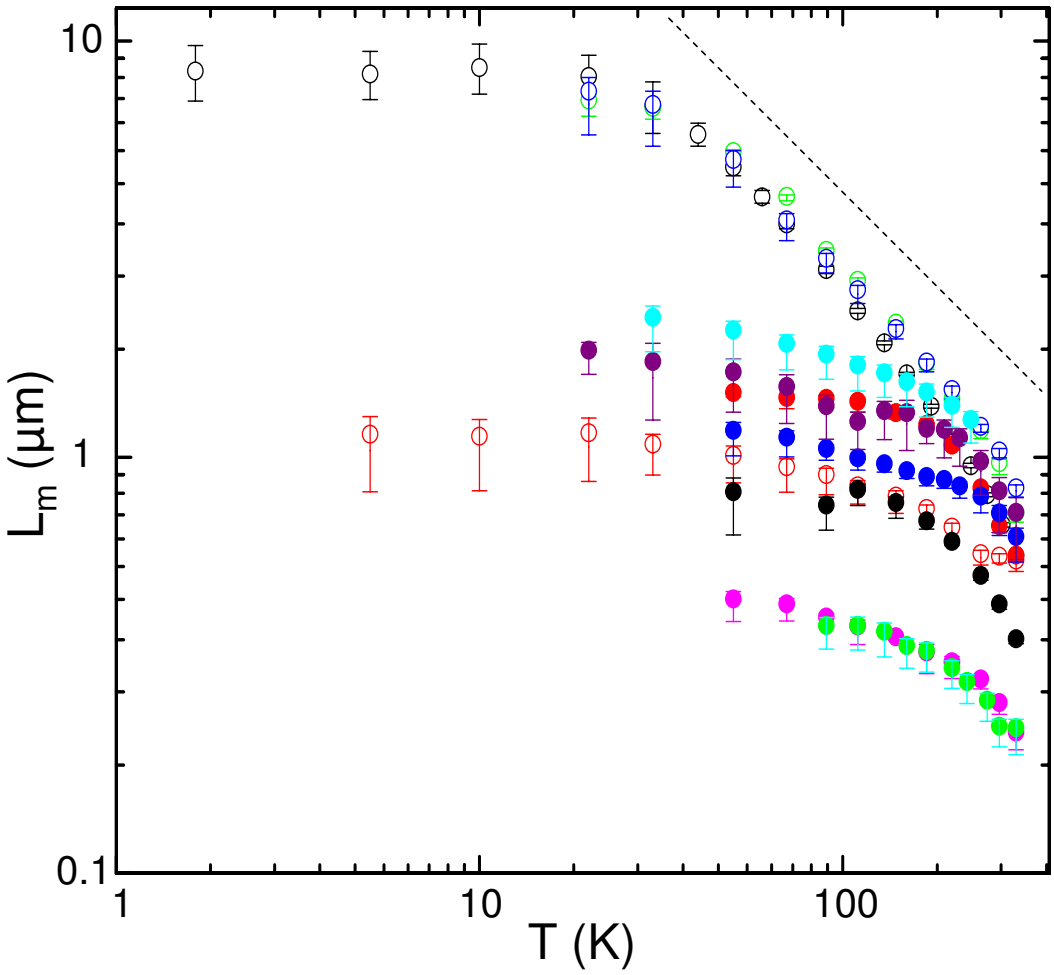

Figure 2.8: The electron mean free path for the samples listed in Table 2.1 at different temperatures. Most metallic SWNTs (open circles) saturate at higher values than that of semiconductors (closed circles). The dashed line represents T^{-1} dependence.

M-NTs, while filled circles are S-NTs. Overall, $L_m(T)$ exhibits different behaviors in two regimes separated by T_{cr}: (i) the high temperature regime ($T > T_{cr}$) where $L_m \sim T^{-1}$ (dashed line in Fig. 2.8) and (ii) the low temperature regime ($T < T_{cr}$) where L_m saturates to the the sample specific L_m^{sat}. Note the strong grouping of L_m's at room temperature and the extraordinarily long values. This is an order of magnitude larger than the mean free path of carriers in the cleanest 2DEGs [15]. The

occurrence of two regimes is the result of two scattering mechanisms that dominate at different temperatures. This is the inelastic scattering with acoustic phonons for $T > T_{cr}$ and elastic scattering with static defects for $T < T_{cr}$. Each contributes to the overall L_m by Mathiesson's rule: $L_m^{-1} = L_{ac}^{-1} + L_{static}^{-1}$ and will be discussed below.

Inelastic Acoustic Phonon Scattering & Temperature Dependence

At higher temperature where $T > T_{cr}$, our data suggests that inelastic scattering between electrons and acoustic phonons are dominant, similar to the observation in Ref. [27]. Since these measurements are performed at low bias ($V_{SD} < 10$ meV), we do not expect any contribution from high energy ($E > 180$ meV) optical phonons. Empirically, the temperature dependence closely follows $L_m \sim T^{-1}$. The only temperature dependence expected in L_m is related to the electron scattering time τ, since $L_{ac} = v_F\tau$, where Fermi velocity v_F is constant in both semiconducting and metallic SWNTs in the degenerate limit ($V_g < -20V$). τ is directly proportional to the acoustic phonon population, which has a $1/T$ dependence [30]. This is the dependence we observe for $T > T_{cr}$ and thus conclude that acoustic phonon-electron scattering is the dominant scattering mechanism.

Theoretical work suggests that the scattering rate from acoustic phonons in SWNTs should depend on diameter and temperature: $\tau^{-1} = \alpha T/d$ [33, 34, 30]. Filling in this expression for τ, we expect the length an electron travels before scattering with an acoustic phonon to be: $L_{ac} = v_f d/\alpha T$. Now, plugging this into Mathieson's Rule with two scattering mechanisms we obtain the full expression for the L_m dependence:

$$L_m^{-1} = L_{static}^{-1} + \alpha T/v_f d \tag{2.1}$$

where L_{static} is the temperature independent static impurity and the second term is the inverse of the temperature dependent acoustic phonon scattering L_{ac}.

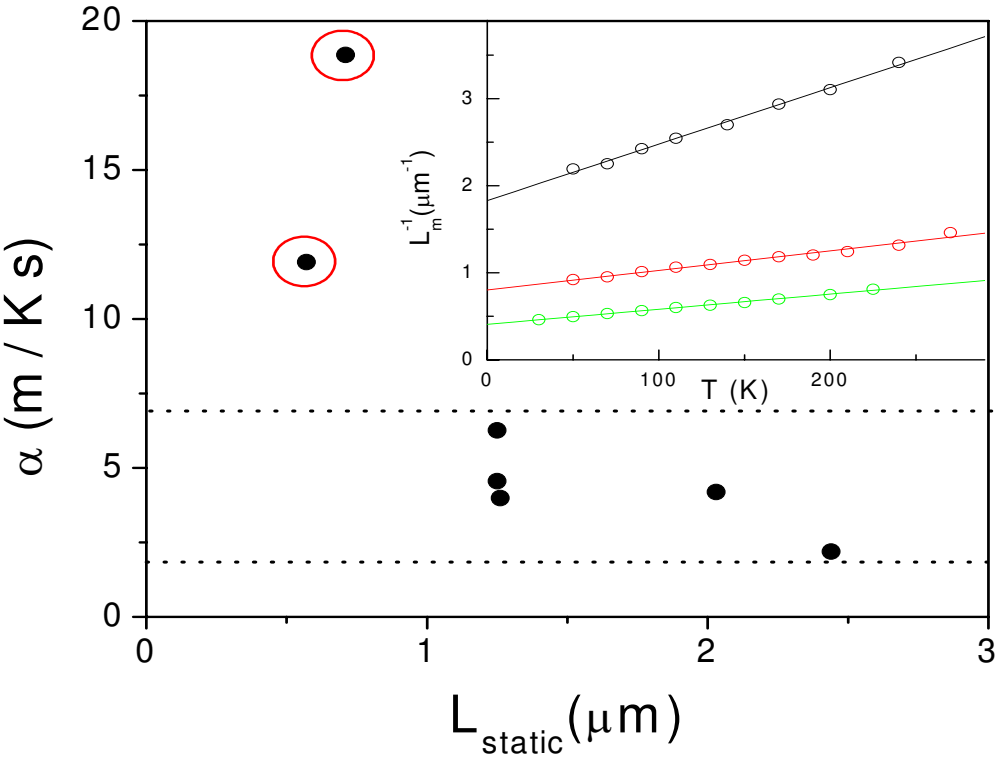

Figure 2.9: (inset) $L_m^{-1}(T)$ for three SWNT samples (circle) and a linear fit (solid line). (main) Besides the two points circled that have anomalously short L_{static}, all values of α appear to be in the 2 - 6.5 m/K·s range (dotted line), with the trend of decreasing α for SWNTs with less impurities.

Thus, $L_m^{-1}(T)$ should be linear with T, with an offset equal to L_{static}^{-1} and a slope multiplied by the diameter and v_f equal to α, as shown in the inset of Fig. 2.9 for three SWNT samples. The main plot in Figure 2.9, shows the obtained α values for each sample as a function of L_{static}. The two data points circled are of anomalously low L_{static}, far smaller than the other 9 samples measured. Three other samples with $L_{static} > 5$ μm are not shown, but are close to the lower dotted line.

Empirically, there is a clear relationship between α and L_{static}: for smaller L_{static}, α becomes larger. Theoretical estimates of α include 6.25 m/K·s by Pennington et al. [33], who solve for the scattering rate analytically using Fermi's Golden Rule

and 1.6 m/K·s by Perebeinos et al. [34], who obtained the scattering rate by numerically solving the Boltzmann equation. The dotted lines in Figure 2.9 represent these values. Both these methods used perfectly clean, defect-free SWNTs in their analysis. Although there is no a priori reason why α should depend on the disorder in the SWNT, we observe that the cleanest samples approach theoretical estimates. An experimental value of $\alpha \approx$10 m/K·s was obtained in Ref. [30]. While they could not explain the discrepancy, our analysis shows that this might be explained by an abundance of impurities in their samples which resulted in a higher estimation of α.

Elastic Defect Scattering & Scanning Gate Microscopy

For $T < T_{cr}$, the acoustic phonon occupation is small and the temperature independent elastic scattering with static impurities becomes more dominant. This scattering determines the value of L_m^{sat}. We believe the widely spread L_m^{sat} values (0.4 - 10 μm) for $T < T_{cr}$ are a result of each SWNT sample having static disorder of different strengths and densities. We employ scanning gate microscopy (SGM)to image this static disorder [35]. Figure 2.10 (a) shows a schematic of the setup. The sample is electrically connected and a small bias V_{SD} is applied while simultaneously measuring I_{SD}. By applying a voltage V_g to the substrate, the Fermi level is tuned so that the device is remains in the threshold region, where conduction is between the on and off state. An electrically conducting AFM tip with an applied voltage, V_{tip}, is brought within 10 nm to a local region of the sample and acts as a local gate. The resulting I_{SD} is recorded as a function of the tip spatial position. The SGM images of select S-NTs are shown in Fig. 2.10(b) and (c). When the negative tip is brought close impurities, I_{SD} increases, indicating that this local region is responsible for the suppression of current. This corresponds to the lighter areas in the diagram. On the SWNTs that we performed SGM on, it was revealed that the SWNT with a shorter L_m^{sat} shows more defects, thus confirming our belief that the upper limit for L_m^{sat} is restricted by the static impurity scattering length.

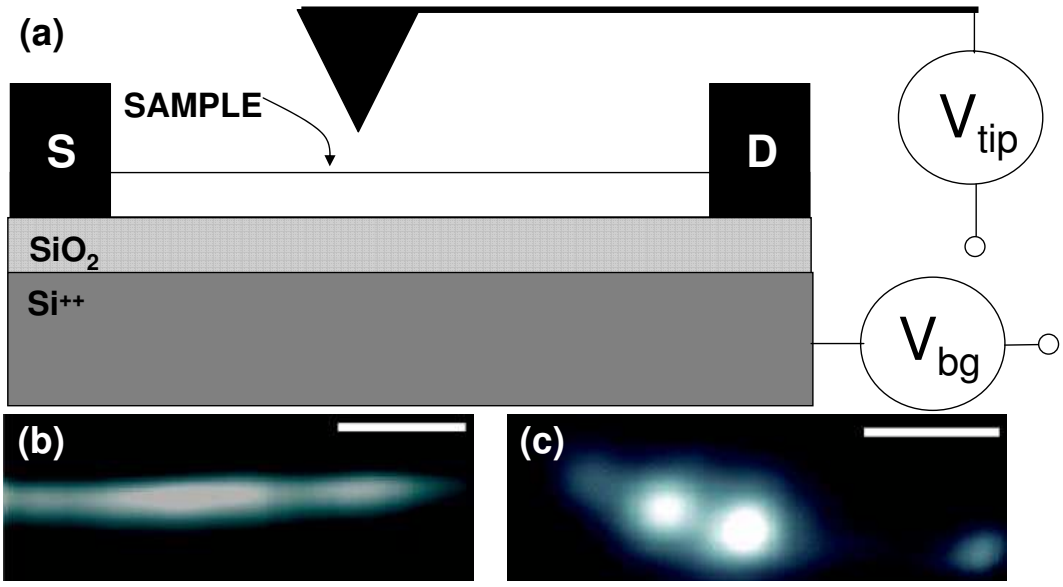

Figure 2.10: (a) Device geometry used when employing Scanning Gate Microscopy on a SWNT. Scanning gate microscopy images taken on devices (b) SC2 and (c) SC7. Lighter color corresponds less current in the SWNT. The defects in the SWNT are highlighted by the bright region (suppressed current) on the SWNT. The scale bar is 500nm.

2.6 Summary

We have experimentally confirmed that L_m is generally much higher for M-NTs than that of S-NTs. This is an indication that the scattering of electrons is strongly suppressed in M-SWNTs, as predicted by Ando et al. [14] and McEuen et al. [36]. In M-NTs, we have experimentally shown that ballistic electron conduction is possible for lengths up to 10 μm at low temperature and even 0.8 μm at room temperature. While L_m is limited at room temperature by inelastic scattering with acoustic phonons, elastic scattering with impurities sets the limit at low temperatures. This is an exciting confirmation of the unusually long scattering length at room temperature (0.8 μm) in SWNTs and is an order of magnitude greater than that measured

in conventional 2DEGs. Thus, the realization of quantum mechanical phenomena at room temperature in SWNTs is a real possibility.

Chapter 3

Non-Linear Scaling of Resistance in Single-Walled Carbon Nanotubes

3.1 Introduction

Background

In the previous chapter, we show that SWNTs have an unusually long electron mean free path as a consequence of the reduced dimensionality [36, 14]. Here, we address a contrasting property of low dimensional materials: the profound effect of disorder. Even small amounts of disorder introduced to the system have large impacts on electron transport [37]. In 1D electrons have no alternative trajectories to circumnavigate defects. Furthermore, as the mean distance between defects becomes comparable to the phase coherence length of the electronic wavefunction, quantum interference effects need to be considered. Previously, we were able to deduce the mean inelastic and elastic electronic scattering lengths from the linear scaling. In this chapter, we discern the effects of static disorder on transport in SWNTs from non-linear scaling. Specifically, we observe that the resistance scales exponentially with channel length for lengths and temperatures beyond sample dependent critical

values.

Effect of Disorder in 1D materials

In an idealization of a solid with a perfect crystalline lattice, an electron wavefunction can be described by Bloch's theorem. This wavefunction has a probability amplitude that extends over the entire lattice and does not scatter as it traverses the conduction channel. In reality, this simple picture breaks down because all materials are far from perfect; translational symmetry of the lattice is generally broken. This may come from lattice vibrations (phonons) that create an asymmetric, dynamic potential landscape. Another mechanism that breaks symmetry is disorder, which can occur in the form of (i) impurities, (ii) defects, such as mono- or di-vacancies, or (iii) external environment, such as trapped charges in the underlying substrate or molecules adsorbed to the surface of SWNTs.

The breaking of lattice symmetry by phonons and disorder result in electron scattering, or in macroscopic terms, resistance. Furthermore, the electron wavefunction becomes non-vanishing for a finite length of the crystal, the localization length L_{loc}. If the electron's phase coherence length, the length which the wavefunction preserves its phase, is comparable to L_{loc}, then the expected transport falls into the Anderson Localization category [18, 6]. A characteristic of this regime is that the resistance scales exponentially with length: $R \sim e^{L/L_{loc}}$.

Previous Experiments and Estimate of L_{loc}

Experiments on understanding disorder in SWNTs has been limited. Bockrath et al. [38] showed that defects, as determined by scanning gate microscopy, are energy dependent scatters. Gao et al. used the temperature dependence of SWNT resistance $R(T)$ to classify the non-linear behavior in terms of variable range hopping [25]. In this case, electrons co-tunnel through a series of quantum dots formed by consecutive defects. In contrast, Gomez-Navarro et al. used the length dependence of SWNT resistance $R(L)$ [17]. They observed an exponential scaling that

they explained in terms of the phase coherent transport phenomena of Anderson Localization. At room temperature, $R(L)$ was measured for lengths up to 2 μm after successive bombardments of the sample with high energy argon ions, which created defects. Each time, more disorder in the form of vacancies was introduced. This resulted in further localization of the electron wavefunction and thus a more steeply exponential scaling, from which they determined $L_{loc} \leq 100$ nm. They used simulations to determine the average spacing between defects, or equivalently, the elastic mean free path. This value multiplied by the number of channels (4 in SWNTs) equaled the experimentally obtained L_{loc}, confirming their observation Anderson Localization in these strongly disordered SWNTs.

3.2 Identifying the Non-Linear Regime in SWNTs

In order to determine whether our non-linear scaling transport data was due to a phase coherent phenomena, we investigate the dependence of resistance on both length and temperature. Fabrication and measurement processes are identical to the method described in the previous chapter. The difference is the inclusion of the non-linear data in our analysis. First, it is necessary to clarify the criterion of the non-linear regime. Figure 3.1(a) is a 3D plot of resistance versus length and temperature for a representative semiconducting SWNT (SC3). Note that the resistance trends in the opposite manner for longer L and lower T than for the shorter L and higher T counterparts.

This is easier to see by taking cross-sections of the 3D plot. For example, $R(T)$ is plotted for fixed L in Figure 3.1(b). The trend below the length dependent critical temperature (in this case $T^* = 50$ K) is in the opposite direction as above T^*. In general, we observe a qualitative dependence of T^* decreasing with L. This is exemplified in Figure 3.1(c), where $R(T)$ decreases for the entire temperature range for data with smaller L. The lack of temperature data points limits the resolution to determine T^* within ± 20 K.

Alternatively, we take cross-sections of Figure 3.1(a) in the other direction by

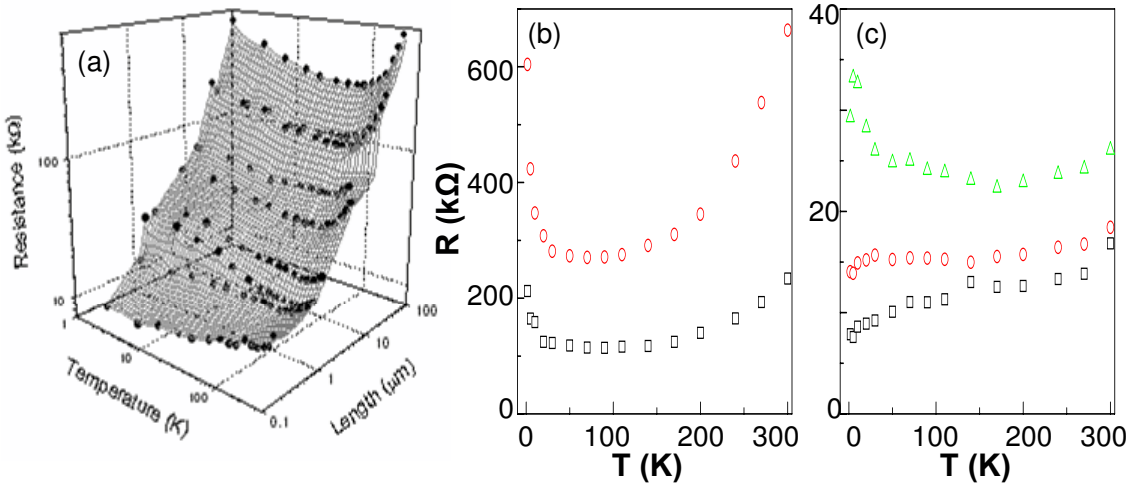

Figure 3.1: (a) 3D plot of resistance as a function of both temperature and channel length for sample SC3. To highlight the general trends, a cross-section $R(T)$ for (b) longer L, which shows a resistance upturn and (c) shorter L, which does not.

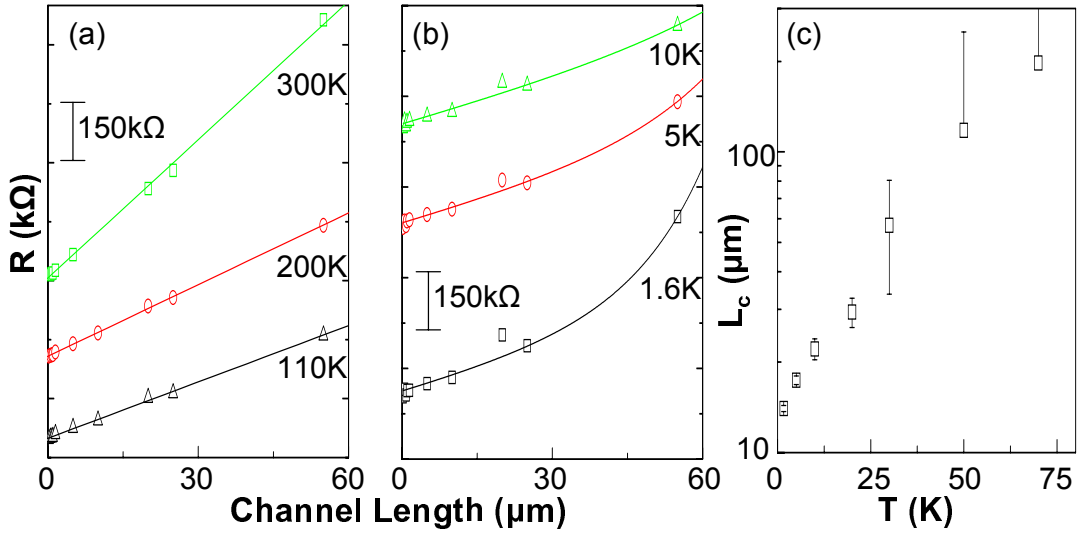

Figure 3.2: The alternative cross-section, $R(L)$, shows (a) linear scaling at higher T. (b) At lower T, the scaling is exponential above critical length scale L_c, which decreases with T (c).

plotting $R(L)$ for fixed T. For this particular sample, the scaling is linear for $T > 110$ K (Fig. 3.2(a)). However, for lower T the longer channel lengths deviate from the linear dependence. To experimentally determine the temperature dependent critical length scale L_c, beyond which non-linear behavior is dominant, we fit the data with a phenomenological equation: $R(L) = R_c + R_Q(L/L_m + e^{L/L_c})$ (solid curves in Fig. 3.2(a) and (b)), where R_c, R_Q, and L_m, are the contact resistance, quantum resistance and electron mean free path, respectively. This is motivated by the expectation that the non-linear behavior is due to Anderson localization. This model uses only L_c as a fitting parameter since all other values are previously determined, as described in Chapter 2. From this fit at each T, L_c is shown to decrease with decreasing T (Fig. 3.2(c)), which is reflected in the increase in non-linearity of $R(L)$ with decreasing T.

3.3 Exponential Scaling of Resistance with Length in SWNTs

We consider two more samples that show non-linear $R(L)$ scaling: a representative metallic (M3) and semiconducting (SC6) SWNT (main panels of Figure 3.3). The deviation from linear behavior may be difficult to see because the data spans over 3 orders of magnitude. To quantitatively address this, we plot $R_{dev} = |R(L) - R_c - R_Q L/L_m|$ at $T = 110$ K (lower inset a) and at $T = 1.65$ K (lower inset b). This is the absolute value of the difference between the actual device resistance and the corresponding linear resistance and thus highlights the extent of the non-linear behavior.

Also plotted for these samples is the critical length L_c which show the same general trend. Firstly, L_c decreases with decreasing temperature. Secondly, $L_c >> L_m$ in all temperature ranges, as shown in Fig. 3.2(c) and the upper insets of Fig. 3.3. This observed behavior of $L_c(T)$ allows us to exclude the phase coherent quantum

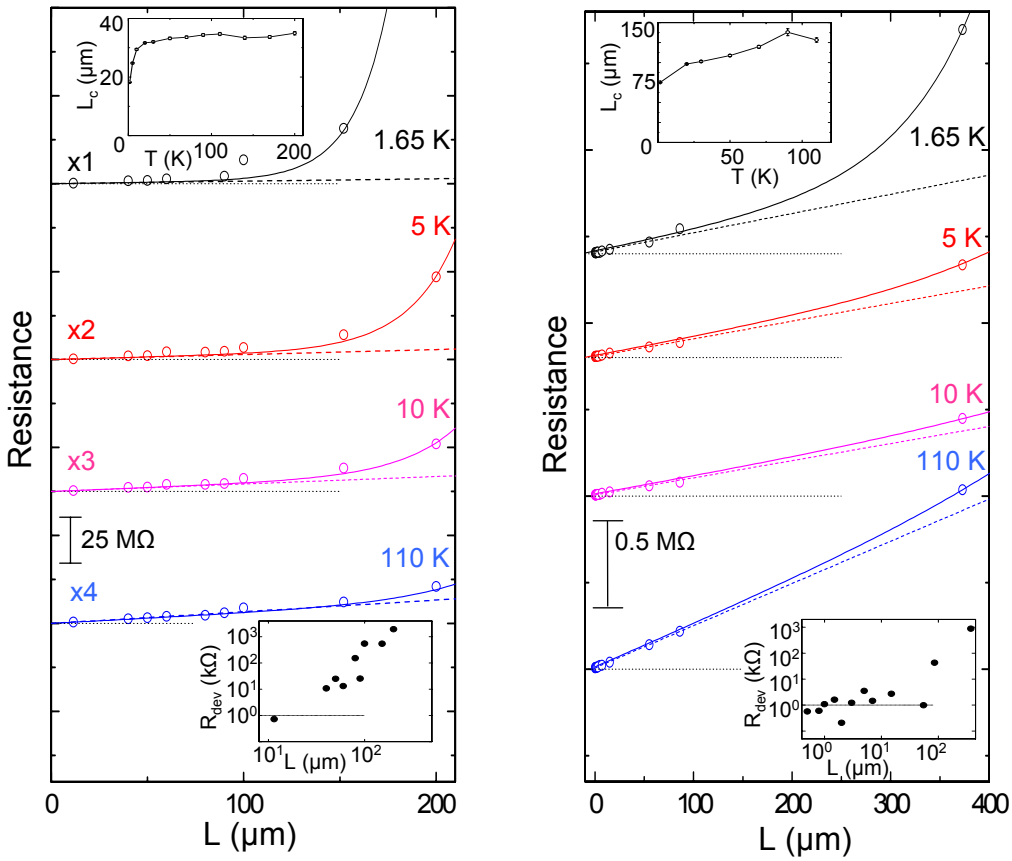

Figure 3.3: $R(L)$ in the non-linear regimes for samples (a) SC6 ($L_m^{sat} \approx 460$ nm) and (b) M3 ($L_m^{sat} \approx 7$ μm). Note that the data is magnified in (a) for clarity. The dashed line is an extension of the linear regime and the solid line is a fit for all data. R_{dev} shows the absolute value of the difference between the actual device resistance and the corresponding linear resistance at 110 K (lower inset a) and 1.65 K (lower inset b). The non-linearity increases with decreasing temperature, which is reflected in the value of L_c(upper insets).

interference of Anderson localization [17] as the reason for non-linear scaling by considering the following argument. At high temperature, the phase coherence length L_ϕ is limited by the inelastic electron-acoustic phonon scattering. Thus $L_\phi \approx L_m$, and are both much smaller than L_c, whereas the opposite behavior expected if

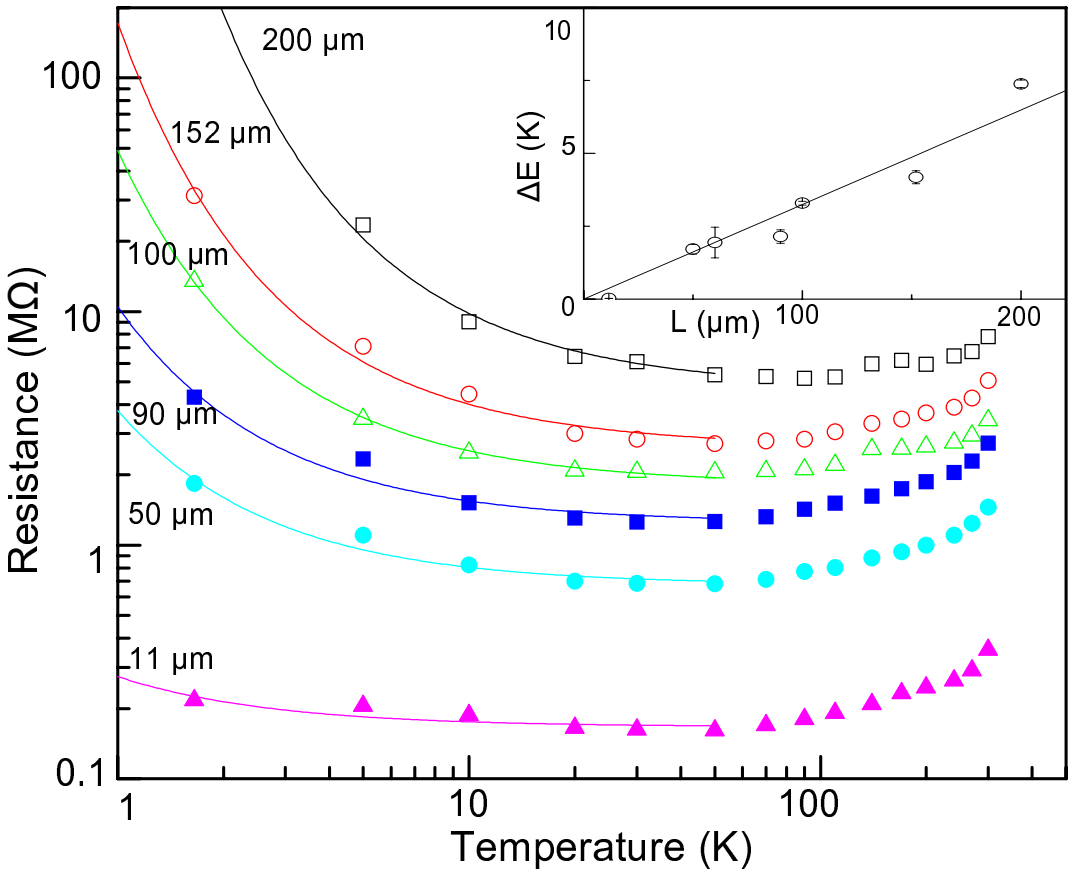

Figure 3.4: $R(T)$ for various channel lengths on the same sample (SC6). Below $T \sim 50$ K, the resistance increases with decreasing T and is best described by activation energy behavior. The solid lines are these exponential fits with a value of the energy barrier ΔE (inset) that increases with channel length.

Anderson Localization was to be observed. While the exponential scaling is apparent and suggests Anderson Localization, this argument clearly indicates otherwise. Hence, we call L_c the "anomalous" localization length and search for alternative explanations for the non-linear behavior in the next section.

3.4 Activation Energy Behavior

From the exponential scaling of $R(L)$, we extract an "anomalous" localization length. To obtain further transport information, we exploit the alternative dimension in our parameter space: we fix channel length L and observe $R(T)$ in the non-linear regime. Chapter 2 addresses the $T > T^*$ regime where a decreasing $R(T)$ reflects the depopulation of acoustic phonons that are primarily responsible for electron scattering. Here, we focus on $T < T^*$, where R increases with decreasing T and ultimately manifests in the non-linear scaling of $R(L)$.

Below T^*, the resistance is described well by an activation behavior: $R = R_o e^{\Delta E/kT}$, where ΔE is the size of the energy barrier in the conduction channel that requires electrons to be thermally activated over. A representative sample (SC6) with the fitted activation behavior equation (solid lines) is plotted on a log-log scale in Fig. 3.4. While the energy barrier ΔE (inset) is sample dependent, the general trend is the same: increasing ΔE for longer L.

We now discuss possible origins for this data. One possible mechanisms for activation behavior is either Schottky or fixed energy barriers at the interface between the metal electrode and semiconducting SWNT. However, in this case ΔE would be the same for all channel lengths, instead of the observed trend, $\Delta\text{E} \propto L$. Moreover, our data is computed for E_F sufficiently away from the energy band gap by tuning V_g to large negative values ($< -30V$). This suppresses any Schottky barriers between the metal electrodes and SWNTs by narrowing the distance an electron needs to tunnel and thus making the probability for tunneling sufficiently high [39]. As for any other contact related barrier, note that R in Figure 3.1(c) approaches the theoretical minimum of $R_q = 6.5k\Omega$, which confirms transparent contact to the SWNT. All devices on the sample were fabricated simultaneously, so we expect similarly transparent contact throughout the sample. Thus, any activation behavior observed is solely due to occurrences in the bulk part of the SWNTs, rather than at the interface between the electrodes and SWNT.

Another possibility that would result in activation behavior involves electron

co-tunneling through a series of quantum dots created by consecutive impurities, a scenario presented by Gao et al. [25]. In this case, the charging energy ($E_c = e^2/C$) of the smallest quantum dot (L_{dot}) in the conduction channel would create the largest barrier and hence determine the overall measured ΔE. For our samples, $E_c \cdot L_{dot}$ is approximately 5 meV$\cdot\mu$m [40]. The largest experimentally obtained value of ΔE in our data is $\sim$0.5 meV, which corresponds to $L_{dot} \geq 5$ μm. On the other hand, from previous analysis on the sample, we estimated the average distance between defects (L_m^{sat}) is on the order of 100 nm. Such a large discrepancy between L_{dot} and L_{stat} make the co-tunneling model an unlikely fit for our data.

Finally, we believe the impediment that limits electron transmission is due to defects with various strengths randomly distributed in the conduction channel. In longer segments, there is more of a likelihood that a stronger defect exists. This qualitatively explains ΔE increasing with channel length and the large sample dependent variation of ΔE, as we will discuss in the next section.

3.5 Multiprobe Experiment

In order to determine the validity of this hypothesis, we divide long semiconducting SWNTs into multiple segments with equal length. Here, we focus on one sample, where we separate a 140 μm long SWNT into 14 sections, each of channel length 10 μm (Fig. 3.5(a)). To be consistent with previous experimental data, we measure the differential conductance at a fixed back gate voltage of -30 V. This keeps E_F sufficiently away from the energy band gap and makes any Schottky barriers at the contacts sufficiently transparent. In a SWNT that is completely defect-free or has a uniform distribution of defects all segments should have identical transport characteristics. With randomly distributed defects the transport characteristics of each segment should differ.

Consistent with our previous observations, device resistance at room temperature is similar for each segment with little variation (Fig. 3.5(b)). However, at lower T, the resistance values are more scattered. In particular, a few segments

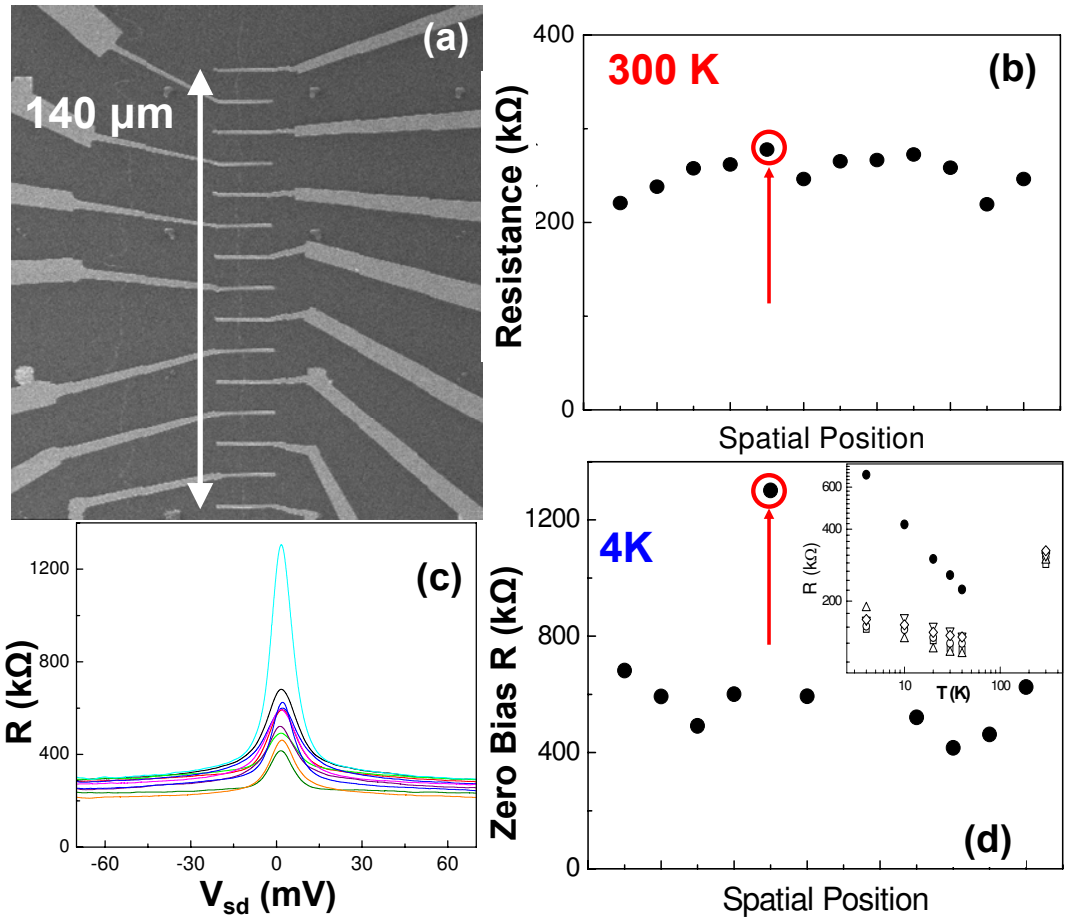

Figure 3.5: (a) A 140 μm long semiconducting SWNT is divided into 14 different 10 μm segments. (b) At room temperature, device resistances are similar, but (c) and (d) at 4 K it becomes more scattered, with one device particularly more resistive than the rest. (Inset) Temperature dependence of R shows the one device diverges from the rest as T decreases.

are much more resistive than the other segments(Fig. 3.5(c) and (d)). The inset of Fig. 3.5(d) shows how the device resistance is tightly grouped at room temperature, but diverges at lower temperature. This data is consistent with our previous assumption that the spatial distribution and the potential magnitude of the defects are randomly distributed. In general, transport in 1D is dominated by the strongest defect in the channel. It also suggests that there are segments of the SWNT that

dominate transport more than others by limiting electron transmission. At higher temperatures, phonons and thermal activation assist the electrons past this defect. At lower T these mechanisms are not present and the SWNTs are more resistive. In longer channel SWNTs, there is more likelihood of strong defects, resulting in more non-linear scaling with length at lower temperature.

3.6 Summary

We presented data on the resistance of SWNTs in the non-linear regime. We showed that while the scaling of $R(L)$ is exponential beyond a critical length scale this is not believed to be related to the phase coherent phenomena of Anderson Localization. Instead, the thermal activation behavior that adequately describes $R(T)$ for $T < T^*$ indicates the non-linear scaling is most likely due to randomly distributed defects with varying strengths. The data from the multiprobe experiment qualitatively corroborates this possibility.

Chapter 4

High Bias Electron Transport in Single-Walled Carbon Nanotubes

4.1 Introduction

Motivation

Carbon nanotubes are promising materials for high performance electronics. They have current carrying capabilities that allow up to 10^9 Amps/cm^2, an order of magnitude larger than conventional metals. The mobility at low fields have been shown to be 79,000 cm^2/V·s, exceeding any other semiconductor at room temperature [41]. Another feature at room temperature is the extraordinarily long mean free path of 1 μm, an order of magnitude longer than the cleanest conventional 2DEGs. At higher fields, the mobility and the mean free path are significantly reduced. To exploit their extraordinary features and use SWNTs as building blocks in nanoscale devices, it is necessary to understand performance limitations imposed at large source-drain voltage V_{SD}.

In Chapters 2 and 3, we discussed electron transport in SWNTs for small V_{SD}, where the applied bias was close to or less than the thermal energy ($eV_{SD} < kT$). We found that scattering was temperature dependent: acoustic phonon scattering at higher temperature and at lower temperatures where the acoustic phonon modes are

depopulated the dominant scattering mechanism is the sample-dependent disorder density. For higher bias, where the applied bias is much greater than the thermal energy ($eV_{SD} \gg kT$), we expect temperature independent phenomena.

Much work has been done to understand electron transport at high bias in metallic SWNTs (m-SWNTs) [22, 42, 27, 43, 44, 7], but relatively few experiments have been performed on semiconducting SWNTs (s-SWNTs) [45] despite intense theoretical interest [34, 33, 46]. Here, we present our results of high bias electron transport on both metallic and semiconducting SWNTs.

Previous Experiments and Estimations of Scattering Length

In his seminal paper, Yao et al. demonstrated that optical phonon emission was the main source of scattering at high bias in metallic SWNTs [7]. It was argued that optical phonon absorption was not present because of its high energy and thus low occupation at room temperature and below ($\hbar\Omega \gg kT$). The emission of optical phonons sufficiently explained the source-drain current saturation of 25 μA for large V_{SD}. On suspended devices, where no substrate is present to serve as a heat sink, the heat generated by high energy scattering creates a non-equilibrium population of optical phonons [43]. In this case, phonon emission and absorption both contribute to the scattering resulting in reduced the current carrying capabilities.

In addition to the current saturation at high bias in m-SWNTs, Yao et al. were able to estimate the optical phonon scattering length, L_o [7]. They fit experimentally obtained current versus source-drain voltage (IV) curves using Boltzmann formulism to estimate $L_o = 10$, although they also used a simple tight binding calculation to obtain $L_o = 100$ nm. While these two estimations are an order of magnitude apart, it provided a rough approximation of the short scattering lengths relative to the acoustic phonon scattering length. Scattering lengths add inversely according to Matheisson's Rule, so it was clear from these estimates that high energy phonons would dominate transport properties of SWNTs at high bias.

Javey, et al. provided similar optical phonon arguments and from experimentally

obtained IV characteristics of m-SWNT with different channel lengths confirmed $L_o = 15$ nm [22]. In addition to this, they were able to observe ballistic conduction for devices with channel lengths shorter than L_o, indicated by the device resistance approaching the quantum limit of 6.5 kΩ. The current for this device exceeded the 25 μA at high bias, indicating the absence of optical phonon scattering.

Park et al. considered the scaling of resistance with length to estimate $L_o \approx 10$ nm. They used the optical phonon deformation potential to theoretically estimate a value for $L_o^{op} = 180$ nm for optical phonon emission and $L_o^{zo} = 30$ nm for a zone-boundary phonon emission. Since both mechanisms contribute to the total scattering length, they used Mattheison's rule to obtain the theoretical value of $L_o = 38$ nm [27], but were unable to reconcile theory with experiment. Sundqvist et. al. also considered the scaling of resistance with length, but for much longer channel lengths up to 6 μm [44]. For fixed voltage, they observed a decrease in resistance after 1 μm.

We explore the high bias resistance scaling with channel length. In our experiment we analyze electron transport in both semiconducting and metallic SWNTs for channel lengths up to 50 μm. Also, we present the data in a variety of formats to elucidate different features of high bias transport.

4.2 Current-Voltage Characteristics at High Bias

To study high bias transport in SWNTs, we use the devices presented in Chapters 2 and 3. Briefly, multiple two-terminal devices with varying channel lengths ranging from 0.8 to 50 μm are fabricated on a Si/SiO_2 that serves as a back gate which can tune the Fermi energy with the application of a voltage V_g. Previously, a sufficiently small source-drain voltage was applied so that the linear response characteristics were measured. These energies were small relative to room temperature, so temperature dependent transport was observed. In comparison, at higher bias the energies exceed the thermal energy so that transport is temperature independent. Thus, unless specified otherwise, all data presented is taken at 1.6 K.

We apply a voltage $V_g = -30$ V so that E_F is sufficiently away from the energy

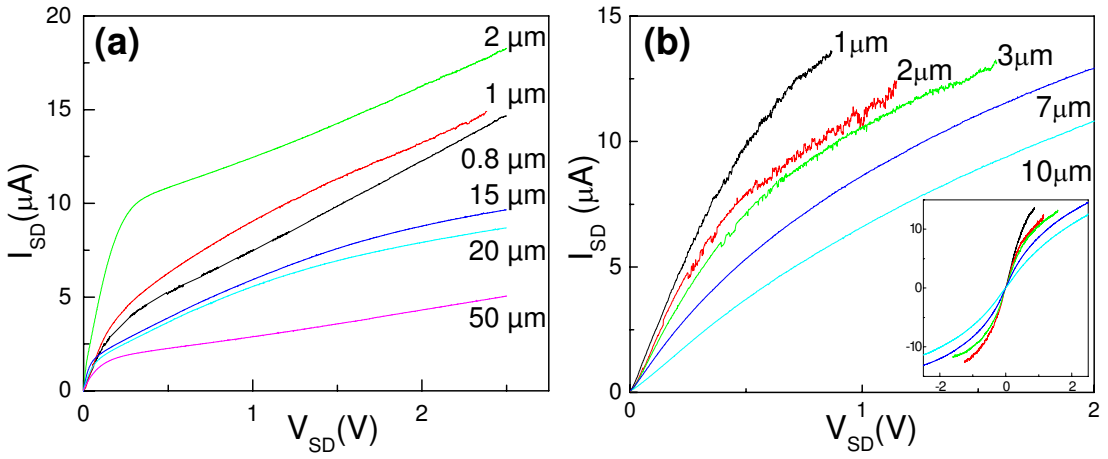

Figure 4.1: DC current I_{SD} measured as a function of applied source-drain voltage V_{SD} for (a) metallic (sample M1) and (b) semiconducting (sample SC5) SWNT at T= 1.6 K. The Fermi energy is tuned sufficiently away from the energy band gap by the application of a back gate voltage $V_g = -30$ V. The inset in (b) shows the IV curves appear symmetric about V_{SD}.

band gap. The DC current I_{SD} is measured as a function of V_{SD} for channel lengths that range from 800 nm to 50 μm. The IV curves are taken for both a metallic (sample M1) and semiconducting (sample SC5) SWNT, as shown in Figure 4.1 (a) and (b), respectively. Unlike a previous report by Chen et al. [45], the s-SWNT shows symmetric behavior for negative and positive V_{SD} and appears to saturate in both directions (inset Fig. 4.1(b)). For both SWNTs, the low bias IV is roughly linear up to 0.2 V, which reflects a constant resistance due to scattering with low energy acoustic phonons, as discussed in the previous chapter where we consider the linear response regime in which transport is voltage independent. In the next section, we discuss transport beyond this regime.

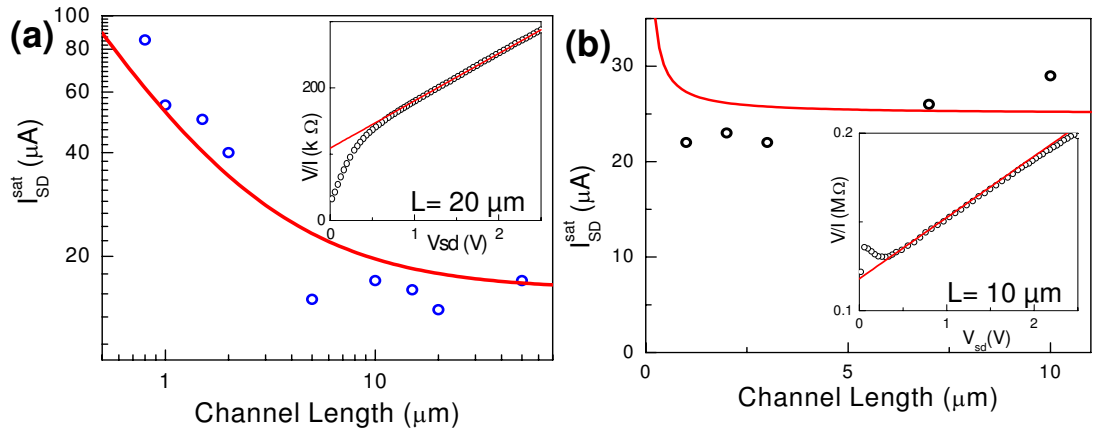

Figure 4.2: For large V_{SD}, the current saturates in both (a) metallic (M1) and (b) semiconducting (SC5) SWNTs. For smaller channel lengths, the electrons reach the energy threshold faster and saturation occurs at higher values. The semi-empirical equation (Eq. 4.2) that governs this behavior is plotted in red. The inset shows the plot of V/I used for estimating I_{SD}^{sat} for specific channel length (a) $L = 20$ μm and (b) $L = 10$ μm. Here, I_{SD}^{sat} is obtained from the inverse of the linear fit.

4.3 Current Saturation

As V_{SD} is increased beyond the linear response for devices with $L > 2\mu$m the I_{SD} clearly appears to saturate (Figure 4.1). In other words, the current becomes constant and the resistance increases with voltage: $V_{SD} = I_{SD}^{sat} R(V)$. For devices shorter than 2 μm, this saturation is less clear unless plotted in a manner that highlights this behavior. It is simplest to estimate by fitting the data with $R(V) = R_o + V_{SD}/I_{SD}^{sat}$ (Figure 4.2 insets). For the shorter lengths, this type of plot allows for a crude estimate of a saturation current, despite the lack of a clear saturation of I_{SD}. The trend for I_{SD}^{sat} in M1 indicates that for smaller channel lengths, the saturation current is higher.

To explain this, we return to the argument for high bias scattering presented by Yao et al. [7]. It was argued that an electron must travel a specific length L_T in an electric field ϵ to gain sufficient energy to emit a phonon. This "threshold" length

L_T is given by:

$$L_T = \frac{\hbar\Omega}{e\epsilon} = \frac{\hbar\Omega}{eV_{SD}}L \tag{4.1}$$

where $\hbar\Omega$ is the energy of the phonon emitted. Once it gains enough energy after traveling L_T, it travels an additional L_o before it emits a phonon. In all, the total mean free path, or distance it travels before scattering, is $L_T + L_o$. The effects of this argument is elucidated by taking limits of the channel length. In the case of long L, Eq. 4.1 shows that L_T is large and the resistance can be written as $R_{long} = (h/4e^2)L/L_T$. Plugging in for L_T and using Ohm's Law, we get the current is: $I_{SD}^{sat} = (4e/h)\hbar\Omega$. This is 25 μA for $\hbar\Omega$ =0.16 eV, which corresponds to the zone-boundary phonon. In the other limit of small channel lengths, L_o is more relevant and $R_{short} = (h/4e^2)L/L_o$, for a current: $I_{SD} = V/[(4e^2/h)(L_o/L)]$, which does not saturate. Combining these two values, we obtain an expression the describes both regimes:

$$I(V)_{SD}^{sat} \approx \frac{4e}{h}\hbar\Omega + \frac{4e^2}{h}\frac{L_o V}{L} \tag{4.2}$$

where the first term is the saturation current I_{SD}^{sat}. We use this equation to fit the data in Figure 4.2 using the empirically observed I_{SD}^{sat} $\approx$16 μA and 25 μA for the metallic and semiconducting SWNTs, respectively. The one parameter fit yields L_o = 95 nm for the metallic and $L_o < 10$ nm for the semiconducting SWNT.

4.4 Electric Field

The channel lengths and resistances of the SWNT devices span many orders of magnitude, so it is convenient to normalize the data so that the quantitative comparison between different devices can be facilitated. This can be done by dividing V_{SD} by the channel length L to obtain the electric field ϵ ($\epsilon = V/L$), which normalizes the total force an applied bias imposes on an electron in the conduction channel. Furthermore, we calculate the resistivity by taking the numerical derivative of the IV

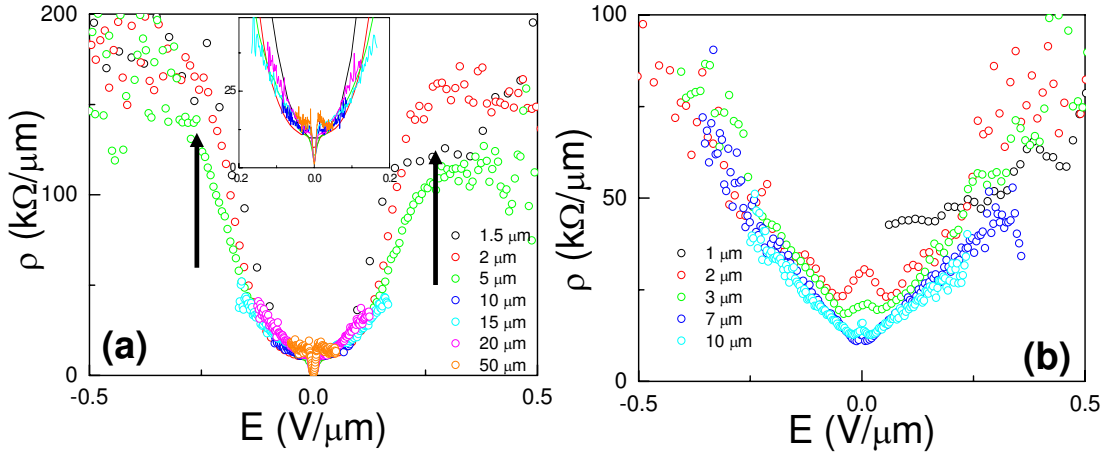

Figure 4.3: The resistivity for each channel length on the same SWNT is equivalent over a range of electric field in (a) metallic (M1) and (b) semiconducting (SC5) SWNT samples. The resistivity increases with increasing field until ϵ_{cr} (arrow), where ρ saturates. In (b), ρ does not saturate, presumably because ϵ is not large enough. The inset in (a) shows a smaller range of ϵ to highlight the overlap of longer length scales.

curves to obtain the differential conductance, $G = dI/dV$. The inverse of this is the differential resistance R, which we scale with length to obtain the 1D resistivity $\rho = dV/dI$. Figure 4.3(a) and (b) show device resistivity versus electric field for M1 and SC5, respectively. As the electric field increases, the SWNT resistivity significantly increases. Figure 4.3(a) shows that ρ increases until $\epsilon_{cr} = 0.3$ V/μm (black arrows), where ρ then saturates to a constant value of $\rho_{sat} \approx 200$ kΩ/μm. In Fig. 4.3(b), crossover to ρ_{sat} is not observed, presumably because ϵ is not large enough. In both cases, all devices for the respective SWNT exhibits the same dependence, implying that resistance scales with length for fixed ϵ and there is a well-defined mean free path L_m. If we follow previous arguments, the increase in ρ at higher ϵ is related to phonon emission. This implies that $L_m = L_T + L_o$ and allows us to write the full expression for $\rho(\epsilon)$, where ϵ is large and beyond the linear regime:

$$\rho(\epsilon) = \frac{R_q}{L_m} = \frac{R_q}{\frac{\hbar\Omega}{e\epsilon} + L_o} \tag{4.3}$$

where R_q is the quantum resistance of $h/4e^2$, $\hbar\Omega$ is the energy of the phonon emitted, and L_o is the mean free path once the electron has sufficient energy to emit the phonon. It is instructive to view this equation in the limit of high and low ϵ:

$$\lim_{\epsilon \to large} \rho = \frac{R_q}{L_o} \tag{4.4}$$

$$\lim_{\epsilon \to zero} \rho = R_q \frac{e\epsilon}{\hbar\Omega} \tag{4.5}$$

Using Equation 4.4, it can be directly surmised that $L_o = R_q/\rho_{sat}$. For $\rho_{sat} \approx$ 200 kΩ/μm, this corresponds to a value of L_o = 33 nm, which is slightly higher than all previous experimental estimates identified in Section 4.1. By equating ρ from the low limit (Eq. 4.5) and high limit (Eq. 4.4) we obtain an expression for the crossover electric field ϵ_{cr}:

$$e\epsilon_{cr} L_o = \hbar\Omega \tag{4.6}$$

where we can plug the experimentally obtained values to the left-hand side of Eq. 4.6 and obtain an estimate of the energy of the phonon emitted by the electron. Using ϵ_{cr}= 0.3 V/μm and L_o = 33 nm, we get $\hbar\Omega$ = 10 meV. This surprising value for $\hbar\Omega$ is an energy in the neighborhood of the radial breathing mode phonon (RBM), which has been shown to be E_{RBM} = 28 meV·nm/d[nm], where d is the diameter of the SWNT. For our samples, d = 2.0 and 2.2 nm for M1 and SC5, respectively. If the scattering was due to optical or zone boundary phonon emission, which has been the basis for most literature on high bias transport in SWNTs (Section 4.1), this would involve $\hbar\Omega \approx$150-200 meV, which we are an order of magnitude away from.

For the applied V_{SD} in our experiments, we certainly expect electrons to interact with phonons of higher energies than the acoustic phonon modes. Verma et al. suggests that for intermediate fields, the RBM mode has a significant impact [47].

Indeed, the values of the V_{SD} used correspond to electric fields below 0.5 V/μm, which Perebeinos et al. suggest is a threshold to observe behavior related to higher energy phonon interaction [34]. On the other hand, some experimental work point to 0.5 V/μm being sufficiently large enough [45]. Note that the theoretical work from Ref. [34] highlights the RBM mode as being the most significant scattering component on the energy scale between acoustic and optical phonons.

The apparent observation of scattering due to the radial breathing mode seems to contradict the observance of current saturation because using the argument of Yao et al. would require $\hbar\Omega$ = 150-200 meV. At this point, we cannot account for this discrepancy. However, we note the ϵ range in Yao et al. is much larger ($\sim$10 V/μm) than the typical fields discussed in this chapter. Further careful study of the cross over electric field range is needed to provide elucidation to this issue.

4.5 Resistance versus Length

Another way to present the data is to observe the resistance for fixed voltage scaling with length (Fig. 4.4), instead of the resistivity scaling with electric field . The scaling is separated into three regimes: (i) small channel length, where scattering is mostly due to high energy phonon emission; (ii) long channel length, where the threshold length for electron scattering is long so that scattering with lower energy acoustic phonon modes is more dominant; and (iii) intermediate length, where scattering by low and high energy phonons is approximately equivalent. For high bias, Park et al. observe only regime (i) because they measured channel lengths shorter than 1 μm. Sundqvist et al. measured channel lengths up to 6 μm for biases of 0.1 to 2 V [44]. They found a general trend of resistance saturation at SWNT channel lengths of 1 μm followed by a decreasing resistance and explained this using a Monte Carlo solution of the one-dimensional Boltzmann's equation.

In our data, we observe no such trend. In fact, the data is well described by the

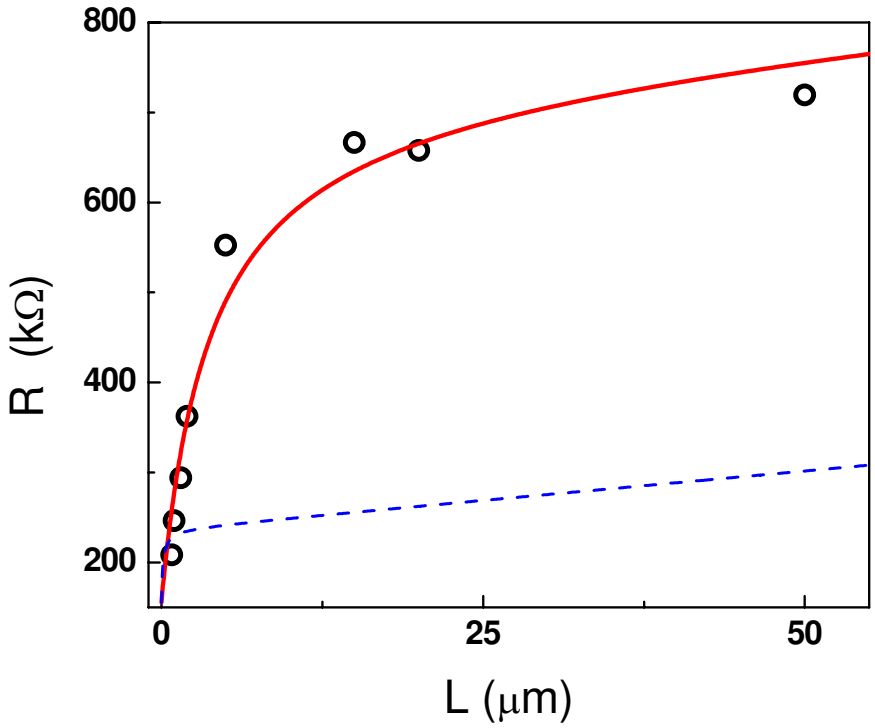

Figure 4.4: For a fixed bias voltage, the slope of the linear resistance scaling with length is more steep for shorter lengths compared to longer lengths. This reflects the short mean free length at stronger fields. The red line is Eq. 4.7 with $\hbar\Omega = 20$ meV and $L_o = 45$ nm showing excellent agreement. For comparison, the blue dashed line is Eq. 4.7 with $\hbar\Omega = 160$ meV.

semi-empirical equation:

$$R = R_q \frac{L}{L_{ac}} + R_q \frac{L}{\frac{\hbar\Omega L}{eV_{SD}} + L_o} \tag{4.7}$$

The first term is the resistance due to acoustic phonon scattering and has been established for this sample, as described in Chapter 2. The second term is Eq. 4.3 multiplied by length and is the resistance due to high bias scattering. This model has two fitting parameters: Ω and L_o. For $\hbar\Omega = 20$ meV and the L_o =45 nm, the red line in Figure 4.4 shows the model fitting to the data with reasonable agreement. In Fig. 4.4 we also plot Eq. 4.7 with $\hbar\Omega = 160$ meV, the energy expected for optical phonon emission (blue dashed line). It is apparent that this energy is not even close

to the observed behavior.

4.6 Conductance Dips in Semiconducting SWNTs

The semiconducting SWNT electron transport data presented thus far is for a Fermi energy in the degenerate regime, far away from the energy band gap (V_g = -30 V). In this regime, the energy dispersion relation is linear and transport is likely to be very similar to that of metallic SWNTs. With E_F closer to the energy band gap of semiconducting SWNTs, significant differences are expected. Firstly, the band curvature results in a larger effective mass and thus slower Fermi velocity. Secondly, for large energy phonon emission, the small momentum emission process involves relaxation across the energy band gap.

To address the possibility of distinct transport phenomena in semiconducting SWNTs, we measure IV relationships with varying V_g, large V_{SD}, T = 1.6 K and different channel lengths L in 3 different samples. The numerical differentiation of the IV curves yields identical results to measuring the differential conductance dI/dV directly. We show the numerically differentiated dI/dV for a representative semiconductor (sample SC5) with channel length of 5 μm in Fig. 4.5(a). For $V_g <$ -12 V, dI/dV show typical electron transport behavior: a decreasing differential conductance with increasing V_{SD}. However, for $V_g >$ -12 V, or equivalently for E_F closer to the energy band gap, a sharp dip appears in the differential conductance for a specific $\pm V_{SD}$. Although resolution depends on the quality of the data, most often there appears to be two consecutive dips, as shown with cross section from the stability diagram in the inset of Fig. 4.5(a). We note that metallic SWNTs showed no such behavior for V_g close to the charge-neutral point, indicating that the conductance dips are a consequence of the energy band gap in semiconducting SWNTs.

From the stability diagram in Figure 4.5(a), it appears that the conductance dips occur at higher V_{SD} as V_g moves closer to the energy band gap. To make quantitative comparisons with other samples and channel length scales, we define

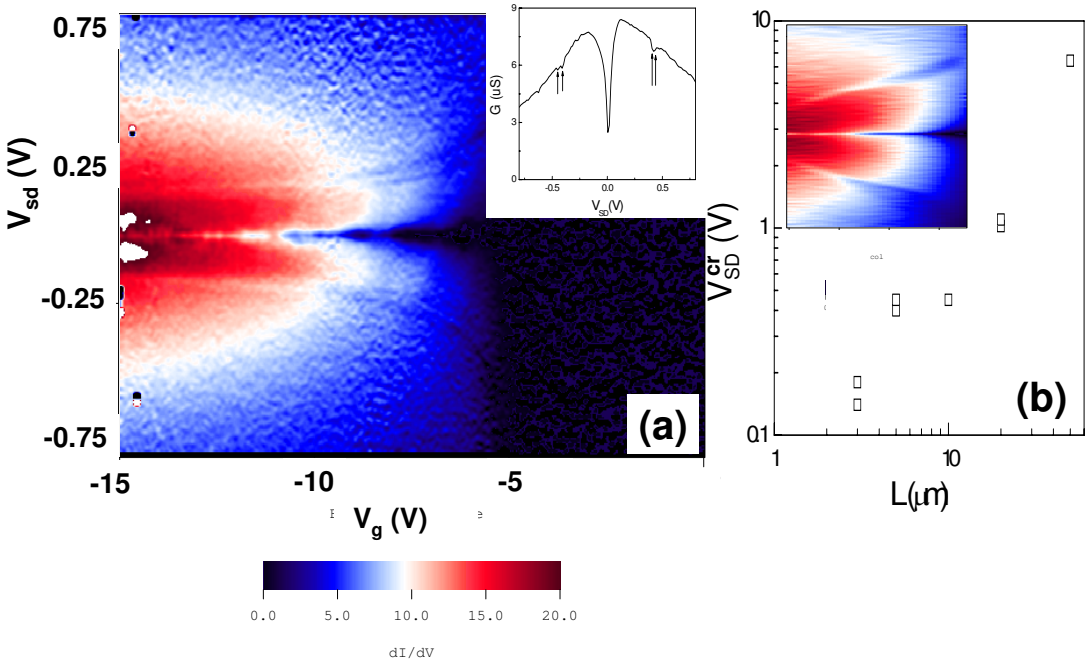

Figure 4.5: (a) Numerical differentiation of IV curves take for different V_g for sample SC5 and channel length $L = 5$ μm. For E_F far away from the energy band gap, typical dI/dV behavior is observed. For E_F closer to the energy band gap, we observe dips in the differential conductance (inset). (b) For three different samples, and channel lengths ranging from 3 to 50 μm, the source-drain voltage $\pm V_{SD}^{cr}$ where the conductance dips are observed scales with length.

V_{SD}^{cr} as the source-drain bias where the dip appears at the V_g where the energy band gap opens up. Interestingly, V_{SD}^{cr} appears to scale with channel length (Fig. 4.5(b)). In other words, the conductance dip occurs at a specific electric field ranging from $\epsilon_{cr} \approx 50$ - 100 meV/μm.

At higher bias such as these, the simple model presented in this chapter presumes that electrons gain energy from the electric field until it reaches a threshold value and emits a phonon. One possible explanation for the conductance dips is that the energy gap in the semiconducting SWNT prohibits electrons to emit phonons because the energy relaxation corresponds to energies inside the gap. For large negative V_g, there

are enough states within the same band to relax to after emission. For V_g closer to the energy gap, V_{SD} must be increased further until states open up within the band, resulting in immediate emission and consequently the conductance dips. On the other hand, observation of this phenomena at such large V_{SD} suggests that its presence should be temperature independent. As we only observe the conductance dips for $T < 1.6$ K, further study is required to determine its origin.

4.7 Conclusion

We measure the electron transport characteristics in a metallic and semiconducting SWNTs at large source-drain bias. In this regime, the resistance scales with length for fixed electric field and in turn suggests a mean free path $L_o > 33$ nm for electric fields ~ 0.5 V/μm, which is two times higher than previous reports [7, 27, 22]. Separate scaling analysis confirms this value and determines that if scattering is indeed a result of phonon emission, the energy of this phonon would be $\sim$10 - 20 meV, corresponding to the radial breathing mode of SWNTs.

Chapter 5

Carbon Nanotube Superlattice

5.1 Introduction

A fundamental principle of solid state physics is the formation of electronic energy bands in a crystal lattice [48]. The free electron model successfully describes several important solid state physics quantities, such as electrical and thermal conductivity. However, it fails to predict the presence of band gaps, or more broadly, metallic and insulating materials. The nearly free electron model makes a modest perturbation by introducing the periodic potential of the crystalline lattice, which qualitatively produces energy bands. More thorough analytical work, like the tight binding model [48], gives a quantitative description of the band structure of materials. Briefly, coupling between discrete individual atomic energy orbitals give rise to a crystal's collective allowed and forbidden energy states. Fig. 5.1(a) shows the element of sodium as an example. As the interatomic distance between isolated sodium atoms decreases, the individual orbitals 1s, 2s, etc. form collective continuous allowed energy bands interrupted by "gaps", or energies for which electrons are forbidden to occupy.

Our experiment aims to artificially mimic this behavior using a superlattice with a 1D single walled carbon nanotube (SWNT) as a host material. A global back gate tunes the electron Fermi energy in the superlattice. For specific energies, transport is

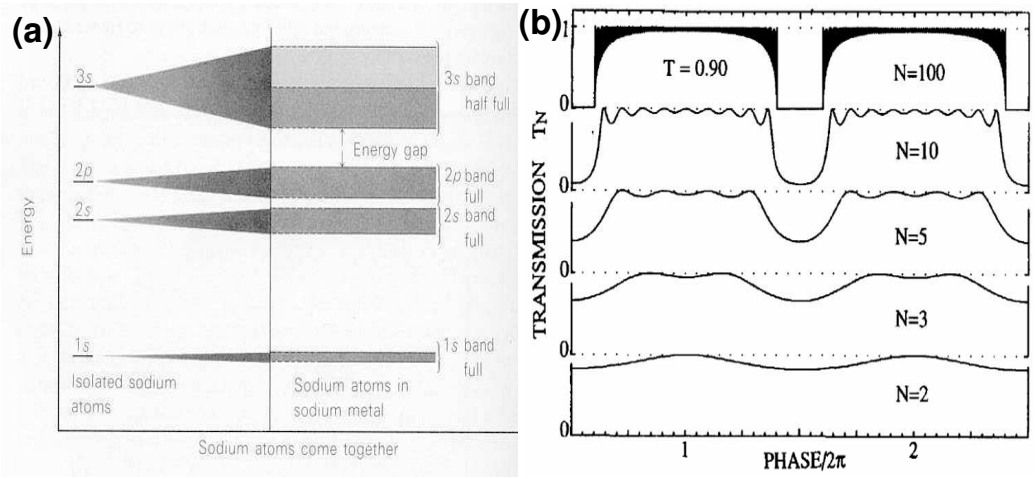

Figure 5.1: (a) As the interatomic distance between individual sodium atoms decreases, the collective ensemble of atoms give rise to allowed and forbidden energies that electrons can occupy. (b) Theoretical calculations of transmission through a 1D superlattice [49]. The distinction between allowed (transmitted) and forbidden (reflected) states increases with the number of barriers (indicated by "N"). For the allowed energy range, or band, the number of oscillations are correlated to the number of barriers as N-1. The phase can be tuned by tuning the Fermi energy with a global back gate.

either allowed or forbidden, which manifests in actual measurements as conductance, which is proportional to the transmission. Transport through the artificial 1-D crystal, or superlattice, can be understood in terms of resonant transmission [50]. Transmission as a function of phase through a superlattice with N barriers (N-1 quantum dots) is calculated in Ref. [49] and shown in Figure 5.1(b). It shows that for a given phase, or equivalently energy, electrons can either pass through or not. For a larger number of quantum dots (QDs), the range of energy (band) where

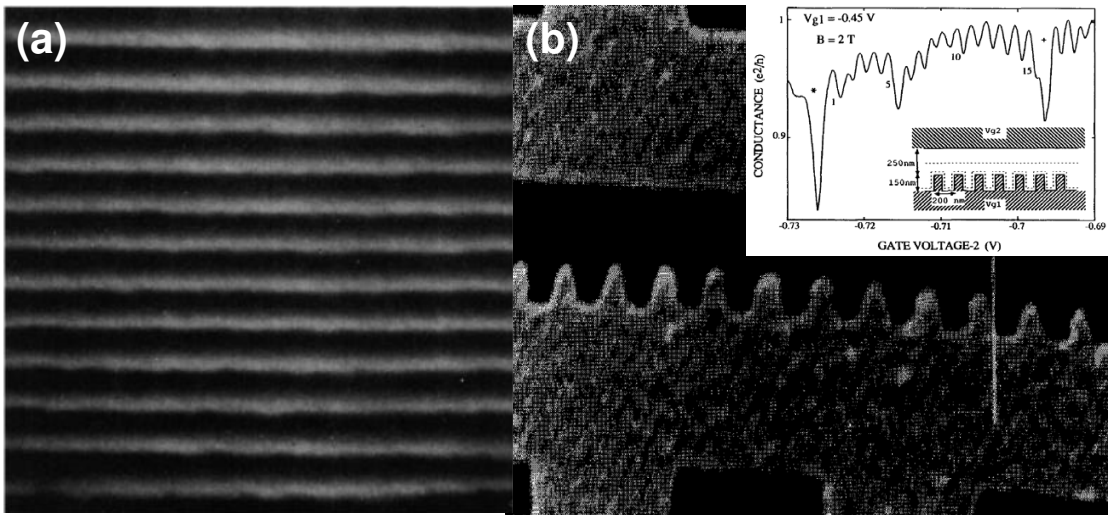

Figure 5.2: Scanning electron microscope image of (a) a GaAs/AlGaAs vertical superlattice fabricated by molecular beam epitaxy (1973 from Ref. [51]) and (b) a GaAs/AlGaAs heterostructure where the top gates define a series of quantum dots on the 2DEG (1990 from Ref. [52]). In (a), the Fermi energy of the system cannot be tuned independently so it must be probed by measuring nonlinear IV transport. In (b), the top gate V_{g2} (inset) tunes the Fermi energy, but also changes the size of the quantum dots, as well as the coupling between them. They observe the number of conductance oscillations to be correlated to the number of dots.

transmission is repressed becomes more distinct. Another notable feature for the allowed band is that the number of observed oscillations and QDs in the structure are equivalent.

5.2 Previous Experiments

The first experimental realization of a superlattice was in 1974 by Esaki and Chang [53]. Here, molecular beam epitaxy was used to fabricate a vertical structure with over 50 periods (Fig. 5.2(a)). They probe the nonlinear transport characteristics of the device by measuring conductance as a function of source-drain voltage and observe conductance oscillations that they believe are a consequence of the superlattice. This is the disadvantage of a vertical structure: there is no way to tune the system's electron Fermi energy collectively so they rely on non-linear transport methods.

Furthermore, the periodicity set by layer thickness and the transmission coefficient between layers are both fixed quantities once the device is fabricated.

Twenty years later, the advancement of semiconductor technology allowed Kouwenhoven, et. al. to improve this geometry [52]. From the 2-dimensional electron gas (2DEG) heterostructure of GaAs/AlGaAs, they were able to create an artificial 1D crystal from a sequence of 15 quantum dots. The dots were defined with 16 "fingers" gates (inset to Fig. 5.2(b) V_{g1}) used to deplete the local region. A second gate V_{g2} was used to control the Fermi energy of the conducting region. Unfortunately, implicit to this geometry, V_{g2} had the additional unwanted consequence of simultaneously reducing dot area and coupling strength between dots. Still, Kouwenhoven et al. were able to observe conductance oscillations as a function of V_{g2} that compared well to the simple model they developed making it apparent that the oscillations arise from the formation of a superlattice's mini-band structure.

There are several benefits of using carbon nanotubes as the host material to make a superlattice. First, it is already a 1D material. Thus, unlike the 2DEGs a global back gate can be independently used to tune the Fermi energy, instead of having the additional duty of reducing the 2DEG channel width. The reduced dimensionality also allows the back gate to not be intimately coupled to other gates in the system. A second reason for using SWNTs as a host material is that single and multiple quantum dot formations have been well studied and are straight forward [9, 54, 55, 56, 57, 58]. Thirdly, the mean free path and phase coherent length can be on the order of microns [34]. Finally, CNTs with lengths >1 cm can be grown [5], so it is possible to fabricate multiple devices on the same SWNT each with a varying number of QDs. As the details of the mini-band structure are dependent on the number of QD's, clear evidence of superlattice behavior can be gleaned by observing the dependence of transport measurements on the number of QDs.

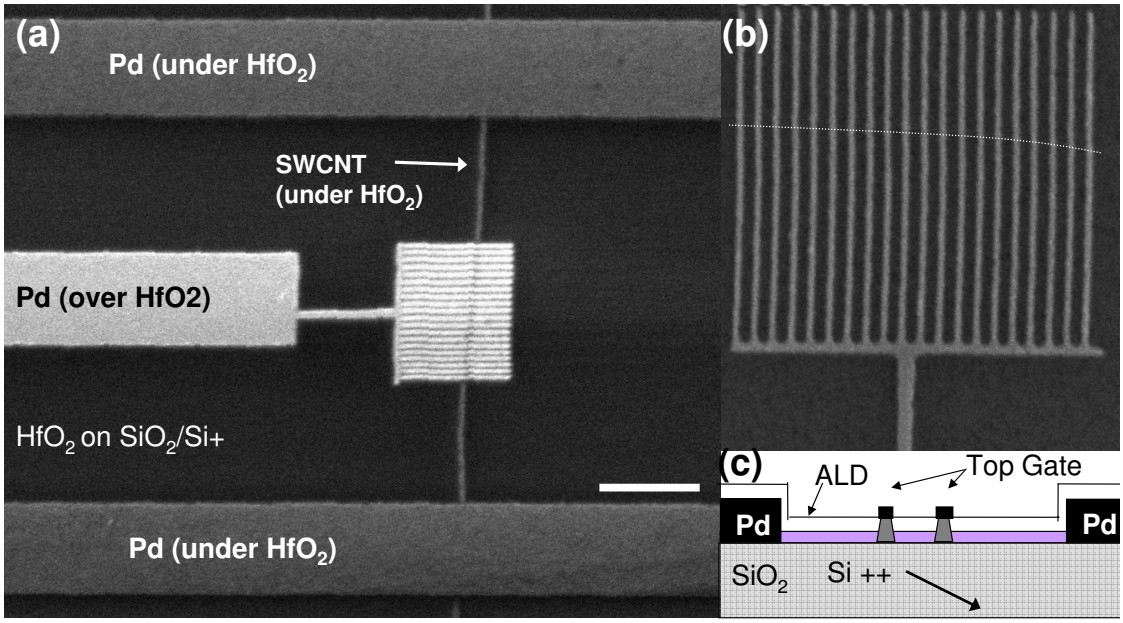

Figure 5.3: (a) A scanning electron microscope image of a two-terminal SWNT device on a Si/SiO_2 substrate, on top of which a 10 nm layer of HfO_2 was deposited using atomic layer deposition (scale bar: 1 μm). Subsequently, a "comb"-like structure was fabricated using ultra-fine lithography (b). The dimensions of the fingers are 20 nm wide with a 60 nm separation. (c) Applying a negative voltage V_{bg} to the back gate induces p-type carriers in the SWNT. Applying a voltage of opposite polarity V_{tg} to the top gate causes local regions directly underneath to act as barriers to the channel (gray). In this case, the region between the two electrodes act as an isolated quantum dot connected to the rest of the SWNT that act as 1D leads.

5.3 Fabrication

The fabrication of a SWNT superlattice requires the formation of a series of quantum dots. A single quantum dot from a metallic SWNT can be formed with tunneling contacts and has been established since the first electron transport experiments were performed [9]. Subsequently, very clean semiconducting quantum dots were shown to have excellent electron-hole symmetry [55]. In order to fabricated multiple quantum dots, top gates that locally deplete the region directly underneath were required [54]. For this reason, we chose to use top gate techniques to define a series of SWNT quantum dots with a lattice spacing of <100 nm, much greater than the lattice spacing in a SWNT crystal (few angstroms).

Ultra-long SWNT were grown on a Si/SiO_2 substrate, which acts as the global gate electrode, as described in Chapter 2. Applying a voltage V_{bg} to the back gate tunes the Fermi energy E_F of the entire electronic system in the SWNT. To compare the effect that tuning V_{bg} has on the transmission through the superlattice with calculations presented in Figure 5.1, we derive the relationship between V_{bg} and ϕ. The change in phase, $\Delta\phi$ is related to the wavenumber k: $\Delta\phi = \int_0^L k\ dx$, where L is the channel length. The dispersion relation relates k_F and E_F: $k = E_F/\hbar v_F$. Finally, the Fermi energy E_F is related to V_{bg} by capacitive coupling: $\Delta E_F = h v_F C_g \Delta V_{bg}/8e$, where e is the electron charge, and C_g is the capacitance per length [40]. Putting this together, we estimate the ΔV_{bg} necessary for $\Delta\phi$=2π:

$$\Delta\phi = \pi L C_g \Delta V_{bg}/4e = 2\pi \tag{5.1}$$

For our samples, C_g ≈15 pF/m [40] and the superlattice channel length is L_{SL}= 1 μm so that ΔV_g ≈1 V. Therefore, we believe that we should observe the full mini-band structure of the superlattice as predicted in Figure 5.1(b) for ΔV_g ≈1 V and all other parameters set appropriately. In our device, V_{bg} serves three independent purposes: (i) eliminate any Schottky barriers that may exist at the palladium electrode-SWNT interface. Thus, the SWNT acts as ideal 1D leads to the superlattice region. (ii) V_{bg} determines the carrier type of the 1D leads (iii) V_{bg} controls the Fermi energy and thus relative phase of the electronic system. The third feature is the most important and can be executed without interfering with the first two tasks by working at a large negative or positive gate voltage.

On top of our substrate and device, a thin layer (10-15nm) of the high-κ dielectric HfO_2 is deposited by Atomic Layer Deposition. We expect that the capacitive coupling of the top gate to be approximately 200 times more effective than the back gate. The HfO_2 dielectric thickness t is 50 times thinner and κ is about 5 times higher ($\kappa \approx 5$ and 25 for Si/SiO_2 and HfO_2, respectively). After HfO_2 deposition, a "comb"-like structure with a specific number of "fingers", or metallic electrodes, are patterned lithographically. Figure 5.3 shows a typical sample with a comb that

has finger width and separation as small as 20 nm and 60 nm, respectively. These remarkably fine structures were fabricated using ultra-fine lithography techniques, as described in Ref. [59]. In brief, a PMMA A2 resist with a thickness of 50 nm is spun on and baked for 10 minutes at 180°. Then electron beam lithography with relatively high dosages of 2000 μC/cm^2 was used to define the fingers. The key to this fabrication is the development: 1 minute in a mixture of isopropyl alcohol and water in a 3:1 ratio at 5°C. Although conditions shifted, this method was generally able to produce features in the range of <100 nm.

Applying a voltage V_{tg} to the local top gate electrodes electrostatically varies E_F directly underneath the electrode. As a result, each electrode serves as a tunable barrier that creates a series of quantum dots with a period of the "comb" structure (80 nm). This periodicity is less than the mean free path SWNTs, which can be over 1μm at low temperatures, thus meeting the requisite for the observation of superlattice transport behavior.

5.4 Measurement

To measure the effects of the superlattice, we would like the phase coherent length and inelastic mean free path to be as long as possible, so we measure at $T = 1.6$ K. Furthermore, all data presented is for the same SWNT, although the number of barriers vary. The device geometry of the SWNT superlattice allows the application of voltages V_{SD}, V_{tg}, and V_{bg}, the source-drain, top gate, and back gate voltages, respectively. From the difference between the Esaki et al. [53] and Kouwenhoven et al. [52] experiments, we know that the most effective method for observing the mini-band structure of the superlattice is in the linear regime. This is accomplished by measuring the zero-bias conductivity with the application of a small AC voltage of 100 μV across the source-drain. A positive (negative) V_{bg} tunes the Fermi energy in the entire SWNT to the conduction (valence) band so that carriers are n-type (p-type). The top gate V_{tg} works in a similar way, but tunes E_F only locally. When V_{tg} and V_{bg} have similar polarities, conduction through the lattice is not suppressed.

However, when they have opposite polarities, the local regions directly underneath the top gate electrodes act as barriers, effectively isolating the regions between the fingers from the rest of the SWNT, (Fig. 5.3). The isolated regions between the fingers are quantum dots that are coupled to each other and on the ends are coupled to the rest of the SWNT, which act as 1D leads.

5.5 Single Quantum Dot

We begin the analysis on a sample that has a channel length of 7 μm and two top gate fingers that act as two barriers which isolate a single quantum dot (Fig. 5.4(b)). We float the voltage to the top gates, to characterize the SWNT in the usual way: measuring the differential conductance as a function of V_{SD}, while stepping V_{bg} (Fig. 5.4(a)). The blue (dark) scale to red (light) scale indicates low to high conductance (full scale range is 0-1 μS). The SWNT energy band gap can be read directly from the diagram, which we estimate to be $\approx$ 50-100 meV. Note the diamonds for positive V_{bg}, which is an indication of coulomb blockade induced disorder in the sample. It can be attributed to either the top gate electrodes acting as scattering mechanisms or more likely, the HfO_2 having charge traps that scatter electrons more than holes (not shown is the relatively more clean p-type conduction). Also noteworthy is that before deposition of HfO_2, the SWNT was strongly p-type, showing a higher conductance for negative V_{bg}. After deposition, the device is more n-type with higher conduction for positive V_{bg}, indicating the atomic layer deposition process dopes the SWNT.

Figure 5.4 (c) shows the zero-bias differential conductance, dI/dV, of a device with for V_{bg} $\pm$ 15 V and V_{tg} $\pm$ 2 V. In the upper right (lower left) quadrant, the 1D SWNT leads and the local regions underneath the top gate electrodes are n-type (p-type). This matching of carrier type results in little or no barrier to the electrons and thus, a relatively high dI/dV (indicated by red, or lighter scaler). For $-10 < V_{bg} < 0$, there is no conduction regardless of V_{tg} because E_F in the SWNT leads lies inside the energy band gap, as can be confirmed in Fig. 5.4(a). In the

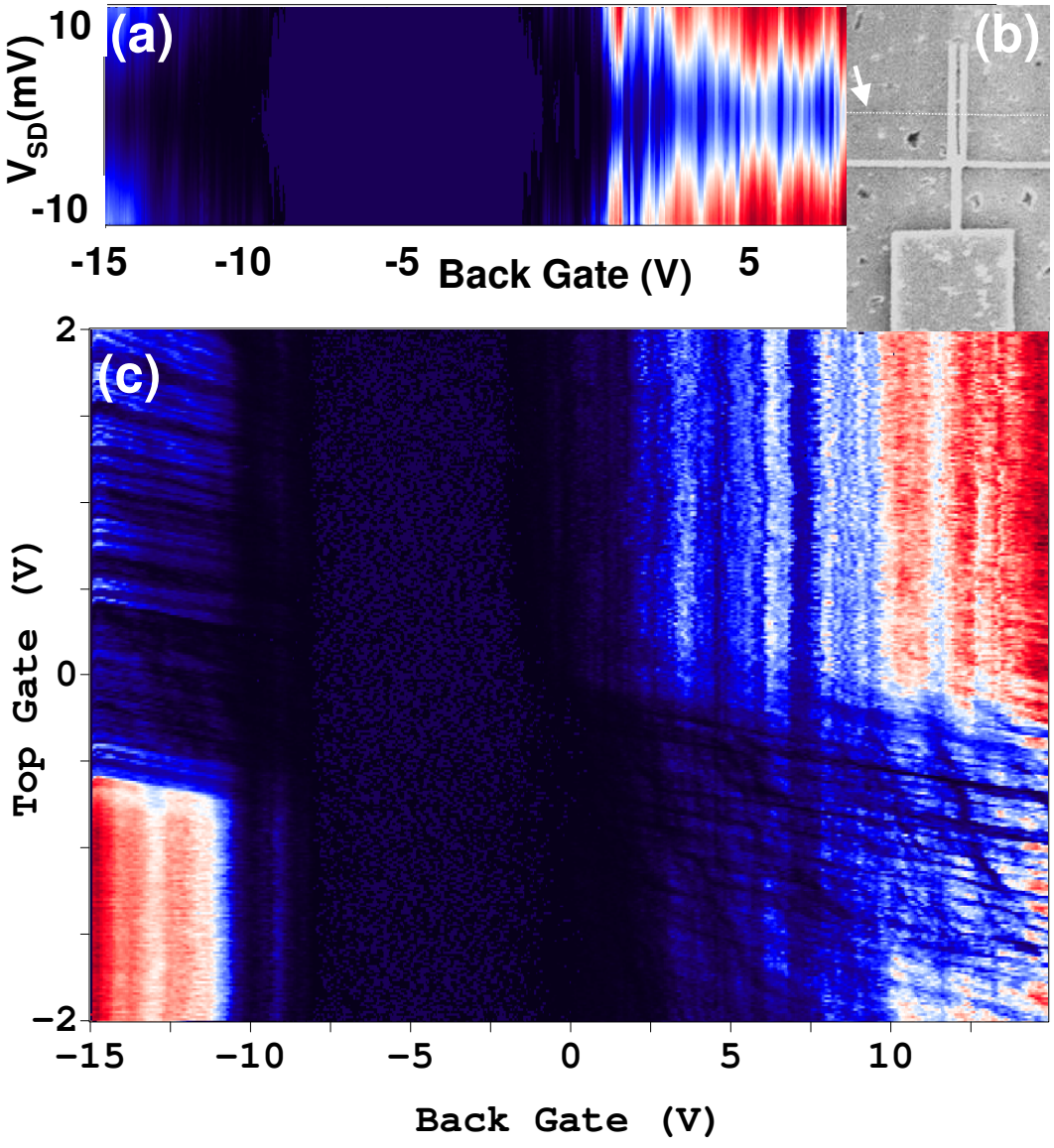

Figure 5.4: (a) Stability diagram for the 2 finger device with V_{tg} floating and a full channel length of 7 μm shows the SWNT to have a small band gap (50-100 meV). Red (lighter) and blue (darker) scale implies high and low differential conductance, respectively, with a full range from 0-1 μS. (b) The two finger top gate forms 1 quantum dot between two metal electrodes that is isolated from the 1D SWNT leads. (c) The zero-bias differential conductance for a range of V_{bg} and V_{tg}. When they have opposite polarity, conduction is suppressed, as tunneling into the quantum dot dominates transport.

upper left (lower right) quadrant, the 1D SWNT leads are p-type (n-type) while the regions underneath V_{tg} are n-type (p-type). This creates a barrier and results in lower dI/dV through the device(indicated by blue, or dark scale).

These two barriers result in a single quantum dot connected to the 1D SWNT leads. The strength of the barriers are related to two parameters: V_{tg} and the size of the SWNT energy band gap. When V_{bg} is sufficiently negative, p-type transport is expected. As V_{tg} is tuned from negative to positive, the Fermi energy directly underneath the electrodes evolves from the valence band to the energy gap and then finally the conduction band. Due to the very small dimension of the top gate (20 nm) and the size of the energy band gap (50-100 meV), the barrier is thin and electrons tunnel through the barrier [60]. Band to band tunneling in SWNTs has been shown to exist with simulations and experiment [61, 62]. This is the case in the upper left quadrant, which we zoom in and analyze further in Fig. 5.5.

For fixed V_{bg}, the differential conductance as a function of V_{tg} shows a four-fold pattern: a large dip, followed by four peaks and then another dip. This four fold pattern is explained in the constant interaction model by the shell filling of the SWNT quantum dot, which successfully describes both "open" [63] and "closed" [56, 57] QDs. Here, "open" or "closed" describes the transparency of the leads to the QDs, where the Kondo effect plays a greater role with more transparency. In this QD, the values of V_{bg} and V_{tg} relative to the energy band gap determines the transparancy. The inset in Fig. 5.5 shows the conductance of a closed dot (lower conductance curve) when V_{bg} = -49 V and is thus closer to the energy band gap. In the case of an open dot (higher conductance curve), when V_{bg} = -53 V, the E_F in the leads are further away. The lower conductance in the closed QD is not related to Schottky barriers at the electrode SWNT interface. Tracing V_{tg} to negative values, where the top gates do not act as barriers, the conductance reaches a maximum value of ≈ 1 μS. The tunable transparency to the QD is an indication that we have control over the barrier strength - a key element to the observation of superlattice behavior.

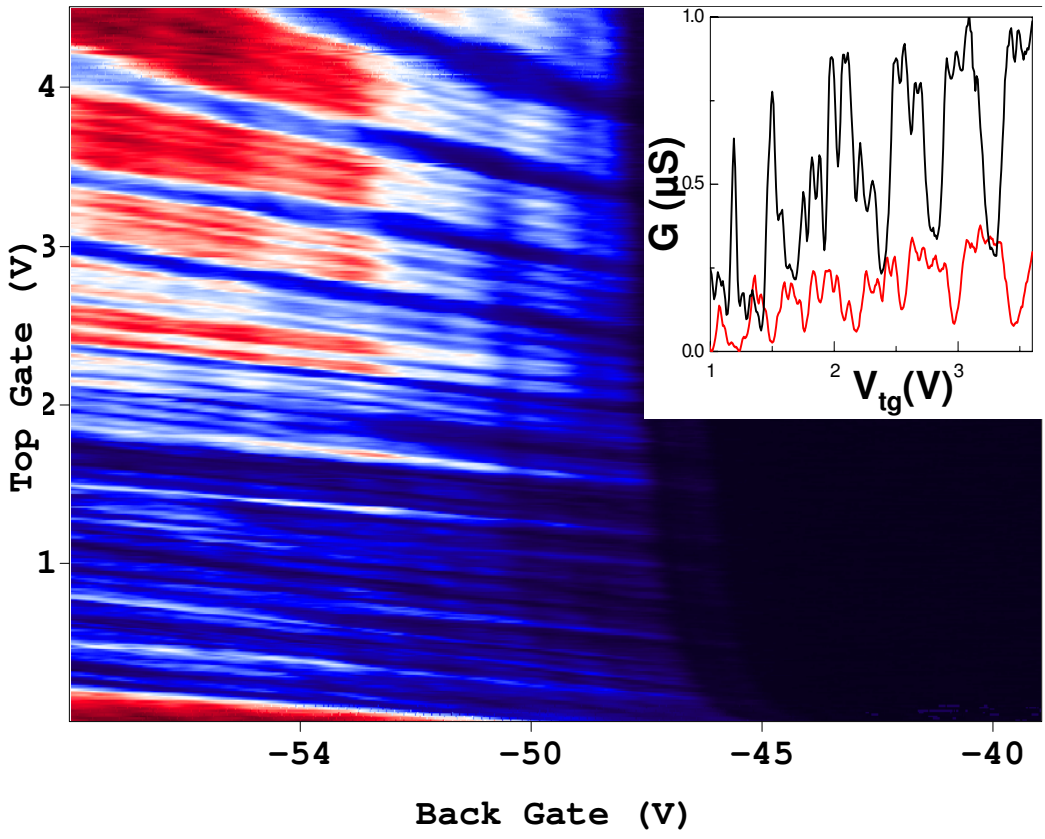

Figure 5.5: The differential conductance measured for the single quantum dot, where V_{tg} and V_{bg} have opposite polarities . Red (lighter) indicates higher conductance and blue (darker) indicates lower conductance, with a full scale range of 0-1 μS. (inset) By tuning V_{bg} and V_{tg} relative to the band gap, the quantum dot can be "closed" (lower conductance curve) or "open" (higher conductance curve). This shows that transparency and thus barrier height to the QD is tunable.

5.6 Multiple Quantum Dots

For the same SWNT sample, multiple two terminal devices were fabricated so that the number of fingers varies on each device, while intrinsic electron transport characteristics of the SWNT remain constant. Here we present data on the same SWNT as the 2 finger device, but with 6 fingers (5 QDs) and 10 fingers (9 QDs). The stability

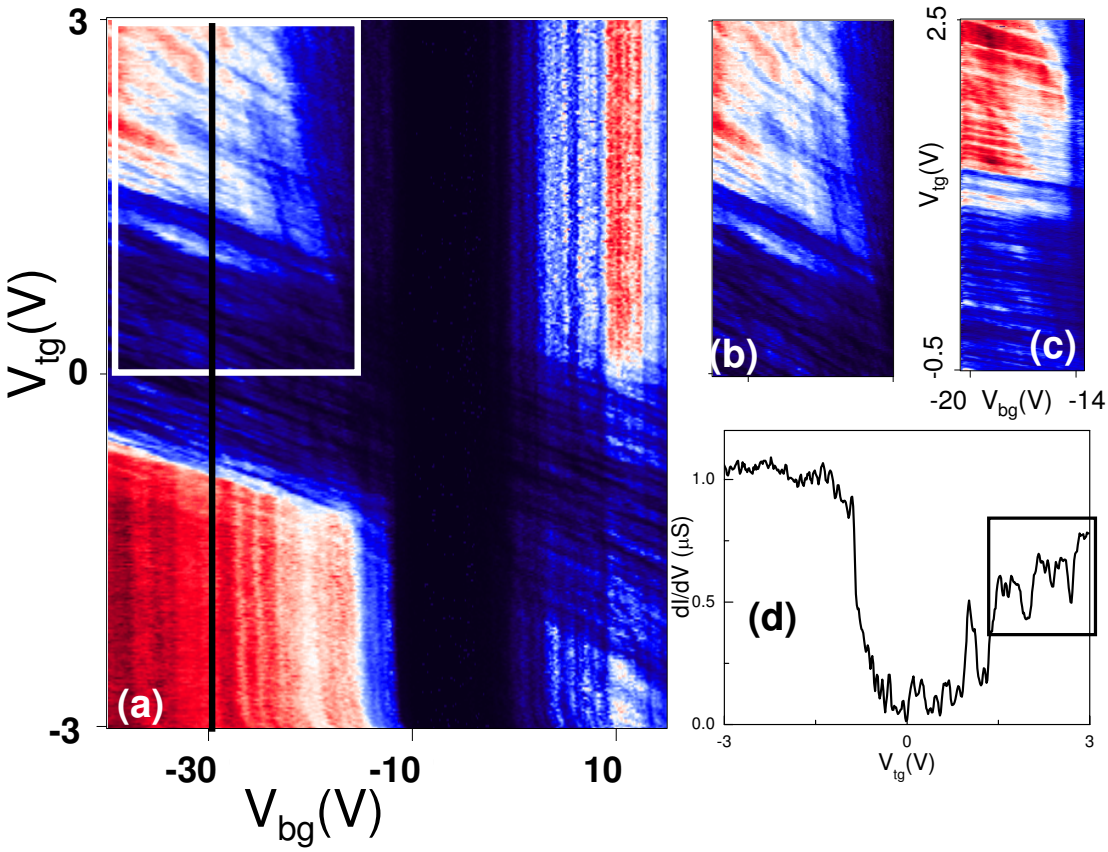

Figure 5.6: (a) Zero-bias differential conductance for a SWNT with 6 fingers (5 QDs). Red (lighter) and blue (darker) scale indicate higher and lower conductance, respectively, with a full scale range of 0-1 μS. Zoom-in of white rectangle area (b) and additional data set (c) shows organized conductance oscillations. Black vertical line in (a) is a cross section highlighted in (d) that shows when V_{tg} has opposite polarity to V_{bg} (black square) the conductance has a period of large dips followed by oscillations, similar to the observation of Kouwenhoven et al. [52].

diagram in Figures 5.6 and 5.7, which correspond to the 6 and 10 finger devices, are both similar to the 2 finger device: when the polarities of V_{bg} and V_{tg} are opposite, conduction is suppressed. Furthermore, the channel length, energy band gap, and capacitive coupling of the top and bottom gates are the same as the previous device. The pattern of conductance oscillations in these suppressed regions, however, is different. The 2 finger, single quantum dot shows oscillations reflecting the shell filling of the 4 orbitals of the SWNT. Multiple dots are expected to be considerably more complicated [54, 58]. Only by increasing the number of QDs beyond three or

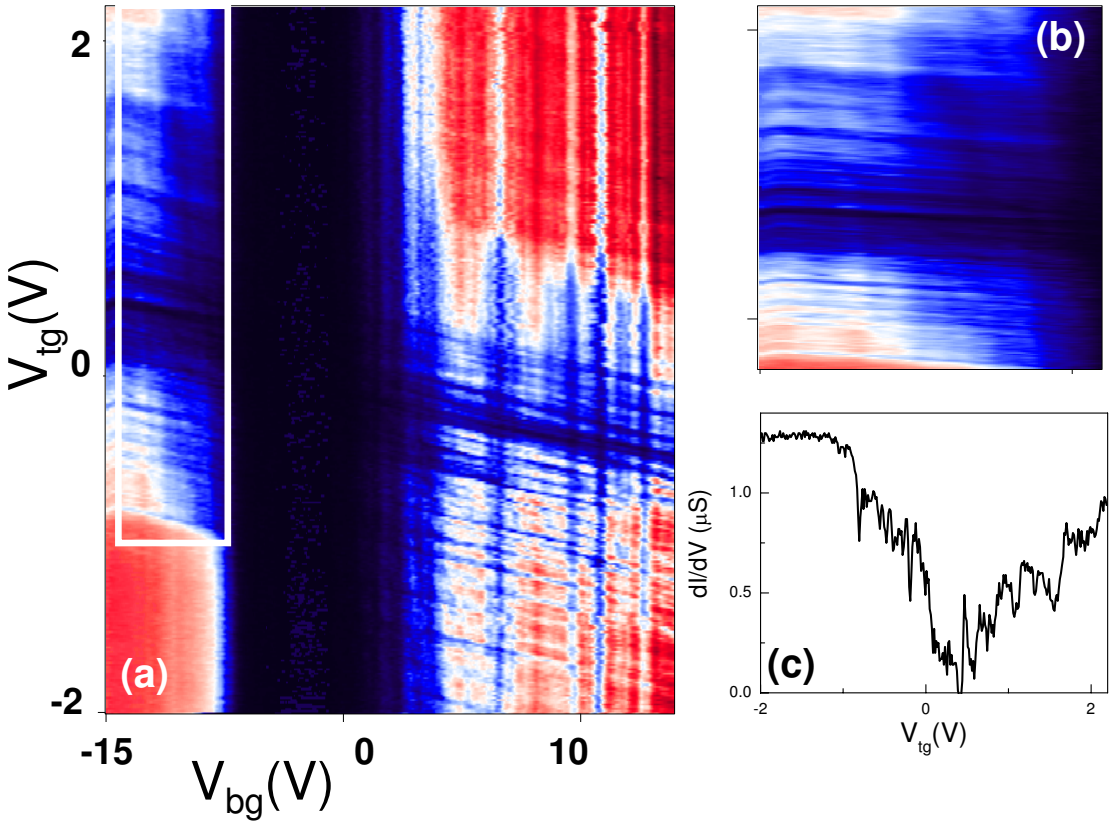

Figure 5.7: (a) Zero-bias differential conductance for a SWNT with 10 fingers (9 QDs). Red (lighter) and blue (darker) scale indicate higher and lower conductance, respectively, with a full scale range of 0-1 μS. Zoom-in of white rectangle area (b) shows organized conductance oscillations. (c) For fixed V_{bg} = -14 V, conductance as a function of V_{tg} shows oscillations for positive V_{tg}.

four, we expect the collective, organized behavior of a superlattice to manifest.

Like the single quantum dot, we focus on the upper left quadrant (Fig. 5.6(b) and (c)), where the carriers in the leads are p-type. Conductance oscillations are apparent by tuning either V_{bg} and V_{tg}. Ideally, measurements can be done such that V_{tg} remains fixed so that the barrier height remains fixed. However, as V_{tg} is about 200 times more effective than V_g in tuning the density (factors of 4.5 and 50, for the dielectric constance and thickness, respectively), the oscillations are much easier to observe in this direction. In this case, E_F in the superlattice structure relative to the E_F in the 1D leads that is tuned so that its band structure is probed. Figure 5.6(d) shows that when V_{tg} is negative the conductance is at a maximum plateau. This

is because the local regions underneath the fingers are in the valence band and do not act as barriers. As V_{tg} becomes more positive, E_F in the local regions enter the energy band gap nd suppress the conductance, then moves into the conduction band, allowing electrons to tunnel through. When V_{tg} is large enough, the conductance shows periods of large dips and then a series of small oscillations, similar to the observation by Kouwenhoven et al. [52]. In the case of the 10 fingers, or 9 quantum dots (see Fig. 5.7), we again observe organized oscillations. However, for both multiple QD configurations, it is not yet possible to glean any quantitative period of oscillation to correlate with the number of quantum dots in the superlattice.

5.7 Conclusion

We successfully fabricated a SWNT superlattice with a period of less than 100 nm using top gates as a way to form multiple (2-10) quantum dots in series. We demonstrate that top gates create effective tunable barriers to a single quantum dot andare able to observe four fold shell filling oscillations corresponding to both a "closed" and "open" quantum dot depending on the magnitude of V_{tg}. In the case of multiple quantum dots, we see a qualitative indication that superlattice behavior is observed.

Bibliography

[1] A. K. Geim and P. Kim. *Scientific American*, 298:68–75, 2008.

[2] H. W. Kroto, J. R. Heath, S. C. O'Brien, R. F. Curl, and R. E. Smalley. *Nature*, 318:162–163, 1985.

[3] Sumio Iijima. *Nature*, 354:56, 1991.

[4] K. S. Novoselov, A. K. Geim, S. V. Morozov, D. Jiang, Y. Zhang, S. V. Dubonos, I. V. Grigorieva, and A. A. Firsovand. *Science*, 306:666, 2005.

[5] B.H. Hong, J.Y. Lee, T. Beetz, Y. Zhu, P. Kim, and K.S. Kim. *J. Am. Chem. Soc.*, 127:15336, 2005.

[6] R. Saito, G. Dresselhaus, and M.S. Dresselhaus. *Physical Properties of Carbon Nanotubes*. Imperial College Press, London, 1998.

[7] Z. Yao, C.L. Kane, and C. Dekker. *Phys. Rev. Lett.*, 84:2941, 2000.

[8] M.S. Purewal, B.H. Hong, A. Ravi, B. Chandra, J. Hone, and P. Kim. *Phys. Rev. Lett.*, 98:186808, 2007.

[9] S.J. Tans, A.R.M. Verschueren, and C. Dekker. *Nature*, 393:49, 1998.

[10] Y. Zhang, J. P. Small, W. V. Pontius, and P. Kim. *Appl. Phys. Lett.*, 86:073104, 2005.

[11] M. Y. Han, B. Oezyilmaz, Y. Zhang, and P. Kim. *Phys. Rev. Lett.*, 98:206805, 2007.

[12] Pablo Jarillo-Herrero. Quantum transport in carbon nanotubes, thesis. 2005.

[13] P.R. Wallace. *Phys. Rev. Lett.*, 71:622, 1947.

[14] T. Ando and T. Nakanishi. *Jpn. J. Appl. Phys.*, 67:1704, 1998.

[15] John H. Davies. *The Physics of Low-dimensional Semiconductors*. Cambridge University Press, 1998.

[16] J. Kong, E. Yenilmez, T.W. Tombler, W. Kim, H. Dai, R.B. Laughlin, L. Liu, C.S. Jayanthi, and S.Y. Wu. *Phys. Rev. Lett.*, 87:106801, 2001.

[17] C. Gomez-Navarro, P.J. de Pablo, J. Gomez-Herrero, B. Biel, F.J. Garcia-Vidal, A. Rubio, and F. Flores. *Nature Materials*, 4:534, 2005.

[18] Supriyo Datta. *Electronic Transport in Mesoscopic Systems*. Cambridge University Press, Cambridge, 1995.

[19] J. Kong, A.M. Casell, and H. Dai. *Chemical Physical Letters*, 292:567–574, 1998.

[20] D. Mann, A. Javey, J. Kong, Q. Wang, and H. Dai. *Nano. Lett.*, 3:1541, 2003.

[21] S. Ilani, L.A.K. Donev, M. Kindermann, and P.L. McEuen. *Nature Phys.*, 2:687, 2006.

[22] A. Javey, J. Guo, M. Paulsson, Q. Wang, D. Mann, M. Lundstrom, and H. Dai. *Phys. Rev. Lett.*, 92:106804, 2004.

[23] A. Javey, J. Guo, Q. Wang, M. Lundstrom, and H. Dai. *Nature*, 424:654, 2003.

[24] W. Liang, M. Bockrath, D. Bozovic, J.H. Hafner, M. Tinkham, and H. Park. *Nature*, 411:665, 2001.

[25] B. Gao, D.C. Glattli, B. Placais, and A. Bachtold. *Phys. Rev. B*, 74:085410, 2006.

[26] B. Gao, Y.F. Chen, M.S. Fuhrer, D.C. Glattli, and A. Bachtold. *Phys. Rev. Lett.*, 95:196802, 2005.

[27] J. Park, S. Rosenblatt, Y. Yaish, V. Sazonova, H. Ustunel, S. Braig, T.A. Arias, P.W. Brouwer, and P.L. McEuen. *Nano. Lett.*, 4:517, 2004.

[28] J. Appenzeller, J. Knoch, V. Derycke, R. Martel, S. Wind, and Ph. Avouris. *Phys. Rev. Lett.*, 89:126801, 2002.

[29] C. Zhou, J. Kong, and H. Dai. *Phys. Rev. Lett.*, 84:5604, 2000.

[30] X. Zhou, J. Park, S. Huang, J. Liu, and P. L. McEuen. *Phys. Rev. Lett.*, 95:146805, 2005.

[31] A. Bezryadin, A. R. M. Verschueren, S. J. Tans, and C. Dekker. *Phys. Rev. Lett.*, 80:4036, 1998.

[32] A. Makarovski, A. Zhukov, J. Liu, and G. Finkelstein. *Phys. Rev. B*, 76:161405(R), 2007.

[33] G. Pennington and N. Goldsman. *Phys. Rev. B*, 68:045426, 2003.

[34] V. Perebeinos, J. Tersoff, and Ph. Avouris. *Phys. Rev. Lett.*, 94:086802, 2005.

[35] A. Bachtold, M.S. Fuhrer, S. Plyasunov, M. Forero, E.H. Anderson, A. Zettl, and P.L. McEuen. *Phys. Rev. Lett.*, 84:6082, 2000.

[36] P.L. McEuen, M. Bockrath, D.H. Cobden, Y. G. Yoon, and S.G. Louie. *Phys. Rev. Lett.*, 83:5098, 1999.

[37] B. Biel, F. J. Garci a Vidal, A. Rubio, and F. Flores. *Phys. Rev. Lett.*, 95:266801, 2005.

[38] Marc Bockrath, Wenjie Liang, Dolores Bozovic, Jason H. Hafner, Charles M. Lieber, M. Tinkham, and Hongkun Park. *Science*, 291:283 – 285, 2001.

[39] S. Heinze, J. Tersoff, R. Martel, V. Derycke, J. Appenzeller, and Ph. Avouris. *Phys. Rev. Lett.*, 89:106801, 2002.

[40] Joshua P. Small, Kerstin M. Perez, and Philip Kim. Modulation of thermoelectric power of individual carbon nanotubes. *Phys. Rev. Lett.*, 91(25):256801, 2003.

[41] T. Durkop, S. A. Getty, E. Cobas, and M.S. Fuhrer. *Nano. Lett.*, 4:35–39, 2004.

[42] Michele Lazzeri, S. Piscanec, Francesco Mauri, A. C. Ferrari, and J. Robertson. *Phys. Rev. Lett.*, 95:236802, 2005.

[43] Eric Pop, David Mann, Jien Cao, Qian Wang, Kenneth Goodson, and Hongjie Dai. *Phys. Rev. Lett.*, 95:155505, 2005.

[44] P. Sundqvist, F.J. Garcia-Vidal, F. Flores, M. Moreno-Moreno, C. Gomez-Navarro, J.S. Bunch, and J. Gomez-Herrero. *Nano. Lett.*, 7:2568, 2007.

[45] Yung-Fu Chen and M.S. Fuhrer. *Phys. Rev. Lett.*, 95:236803, 2005.

[46] Debdeep Jena. *condmat0804.3997*, 2008.

[47] A. Verma, M.Z. Kauser, and P.P. Ruden. *Appl. Phys. Lett.*, 87:123101, 2005.

[48] N.W Ashcroft and N.D. Mermin. *Solid State Physics*. Thomas Learning, Inc., 1976.

[49] L.P. Kouwenhoven. *Dissertation*. TU Delft, 1992.

[50] R. Tsu and L. Esaki. *Appl. Phys. Lett.*, 22:562, 1973.

[51] L. L. Chang, L. Esaki, W. E. Howard, R. Ludeke, and G. Schul. *Journal of Vacuum Science and Technology*, 10:655–662, 1973.

[52] L. P. Kouwenhoven, F. W. J. Hekking, B. J. van Wees, C. J. P. M. Harmans, C. E. Timmering, and C. T. Foxon. Transport through a finite one-dimensional crystal. *Phys. Rev. Lett.*, 65(3):361–364, 1990.

[53] L. Esaki and L. L. Chang. New transport phenomenon in a semiconductor "superlattice". *Phys. Rev. Lett.*, 33(8):495–498, 1974.

[54] M. J. Biercuk, S. Garaj, N. Mason, J. M. Chow, and C. M. Marcus. *NanoLett*, 5:1267–1271, 2005.

[55] Pablo Jarillo-Herrero, Sami Sapmaz, Cees Dekker, Leo P. Kouwenhoven, and Herre S. J. van der Zant. *Nature*, 429:389–392, 2004.

[56] David H. Cobden and Jesper Nygard. *Phys. Rev. Lett.*, 89:046803, 2002.

[57] S. Sapmaz, P. Jarillo-Herrero, J. Kong, C. Dekker, L.P. Kouwenhoven, and H.S.J. van der Zant. *Phys. Rev. B*, 71:153402, 2005.

[58] M. J. Biercuk, N. Mason, and C. M. Marcus. *NanoLett*, 4:1–4, 2004.

[59] W. Hu, K. Sarveswaran, M. Lieberman, and G. H. Bernstein. *Journal of Vacuum and Science Technology*, 22:1711–1716, 2004.

[60] J. Appenzeller, M. Radosavljević, J. Knoch, and Ph. Avouris. Tunneling versus thermionic emission in one-dimensional semiconductors. *Phys. Rev. Lett.*, 92(4):048301, 2004.

[61] J. Appenzeller, Y.-M. Lin, J. Knoch, and Ph. Avouris. Band-to-band tunneling in carbon nanotube field-effect transistors. *Phys. Rev. Lett.*, 93(19):196805, 2004.

[62] A. Javey, R. Tu, D.B. Farmer, J. Guo, R.G. Gordon, and H. Dai. *NanoLett*, 5:345–348, 2005.

[63] Wenjie Liang, Marc Bockrath, and Hongkun Park. *Phys. Rev. Lett.*, 88:126801, 2002.